HHS Public Access

Author manuscript

Neuron. Author manuscript; available in PMC 2021 February 05.

Published in final edited form as:

Neuron. 2020 February 05; 105(3): 549–561.e5. doi:10.1016/j.neuron.2019.10.033.

Vasomotion as a driving force for paravascular clearance in the awake mouse brain

Susanne J. van Veluw, PhD[1,2,4,*], **Steven S. Hou, PhD**[2], **Maria Calvo-Rodriguez, PhD**[2], **Michal Arbel-Ornath, PhD**[2], **Austin C. Snyder, BS**[2], **Matthew P. Frosch, MD PhD**[2,3], **Steven M. Greenberg, MD PhD**[1], **Brian J. Bacskai, PhD**[2]

[1]J. Philip Kistler Stroke Research Center, Department of Neurology, Massachusetts General Hospital and Harvard Medical School, Boston, MA 02114, USA

[2]MassGeneral Institute for Neurodegenerative Disease, Massachusetts General Hospital and Harvard Medical School, Charlestown Navy Yard, MA 02129, USA

[3]Neuropathology Service, C.S. Kubik Laboratory for Neuropathology, Massachusetts General Hospital and Harvard Medical School, Boston, MA 02114, USA

[4]Lead Contact

Summary

Paravascular drainage of solutes including amyloid β (Aβ) appears to be an important process in brain health and diseases such as Alzheimer's disease (AD) and cerebral amyloid angiopathy (CAA). Yet, the major driving force for clearance remains largely unknow. Here, we used *in vivo* two-photon microscopy in awake head-fixed mice to assess the role of spontaneous vasomotion in paravascular clearance. Vasomotion correlated with paravascular clearance of fluorescent dextran from the interstitial fluid. Increasing the amplitude of vasomotion by means of visually evoked vascular responses resulted in increased clearance rates in the visual cortex of awake mice. Evoked vascular reactivity was impaired in mice with CAA, which corresponded to slower clearance rates. Our findings suggest that low frequency arteriolar oscillations drive drainage of solutes. Targeting naturally occurring vasomotion in patients with CAA or AD may be a promising early therapeutic option for prevention of Aβ accumulation in the brain.

eTOC Blurb

*Correspondence: svanveluw@mgh.harvard.edu.

Author Contributions

Conceptualization, S.J.v.V., M.A-O., S.M.G., M.P.F., and B.J.B.; Methodology, S.J.v.V.; Software, S.S.H.; Formal Analysis, S.J.v.V. and M.A-O.; Investigation, S.J.v.V., M.C-R., M.A-O, and A.C.S.; Data Curation, S.J.v.V. and S.S.H.; Writing – Original Draft, S.J.v.V.; Writing – Review & Editing, S.J.v.V., M.C-R., S.M.G., and B.J.B.; Visualization, S.J.v.V.; Supervision, S.G.M., and B.J.B.; Funding Acquisition, S.J.v.V., S.M.G., and B.J.B.

Declaration of Interests

The authors declare no competing interests.

Supplemental Data

Supplemental Information including 7 figures and 2 videos can be found with this article online.

Van Veluw et al. demonstrate that vasomotion is a major driving force for paravascular clearance of solutes from the brain. Loss of vascular smooth muscle cells and reduced vasomotion in the context of amyloid deposition is associated with impaired clearance.

Keywords

vasomotion; perivascular space; intra-mural peri-arterial drainage; glymphatics; vascular smooth muscle cells; cerebral amyloid angiopathy; functional hyperemia; Alzheimer's disease

Introduction

Drainage of soluble waste products from the interstitial fluid (ISF) of the brain seems to be an important process to maintain brain health during aging (Xie et al., 2013; Kress et al., 2014; Benveniste et al., 2019). Experimental studies have identified pathways in rodents that drain solutes along vessels into the recently (re-)discovered dural lymphatics, which eventually drain in peripheral lymph nodes (Carare et al., 2008; Louveau et al., 2015; Absinta et al., 2017; Albargothy et al., 2018). Several routes for drainage along vessels have been proposed including the glymphatic system and the intra-mural peri-arterial drainage pathway, which have been described in detail elsewhere (Bakker et al., 2016; Iadecola et al., 2017; Benveniste et al., 2019) and here generally referred to as 'paravascular' clearance. Paravascular clearance is believed to be impaired in patients with brain diseases related to amyloid β (Aβ) accumulation: Alzheimer's disease (AD) and cerebral amyloid angiopathy (CAA) (Weller et al., 2000; Weller et al., 2009; Peng et al., 2016). CAA is characterized by the accumulation of Aβ in leptomeningeal arteries and cortical vessels (Vinters et al., 1987). CAA involves impaired paravascular clearance and Aβ build-up alongside basement membranes within vessel walls, ultimately resulting in ischemic lesions, microhemorrhages, and sometimes fatal large bleeds (Charidimou et al., 2017). Despite its importance in understanding brain health, aging, and disease, the underlying mechanisms that promote paravascular clearance in the brain remain largely unknown. Previous studies suggested that pulsatile blood flow may be a major driving force for clearance (Schley et al., 2006; Iliff et al., 2013), although others have argued that arteriolar pulsations alone are too weak to drive clearance (Diem et al., 2017). An important alternative motive force is much slower and higher amplitude arteriolar oscillations, such as vasomotion (Diem et al., 2017; Albargothy et al., 2018; Aldea et al., 2019). Vasomotion has been described as vascular smooth muscle cell (SMC)-initiated spontaneous vasoconstrictions and -dilations that happen at low frequencies (centered near ~0.1 Hz) and occur relatively independent of pulsatile blood flow (Mateo et al., 2017; Noordmans et al., 2018; He et al., 2018). Understanding the driving force behind paravascular clearance is particularly important for elucidating the pathogenesis of AD, as vascular dysfunction due to CAA can potentially create a self-reinforcing cycle by which progressively worsening vascular dysfunction further diminishes Aβ clearance and promotes deposition.

The aim of the present study was to elucidate the role of vasomotion in paravascular clearance of solutes in the mouse brain *in vivo*. We studied the relationship between spontaneous vasomotion and decay of fluorescent dextrans alongside arterioles with *in vivo*

two-photon microscopy in awake head-fixed transgenic mice with and without vascular Aβ deposition. The effect of increased vasomotion on paravascular fluorescent decay rates was determined utilizing visually-evoked responses (*i.e.* functional hyperemia) in the visual cortex of awake mice. Our results support a key role of vasomotion and thus have direct implications for therapeutic options directed towards the removal of Aβ from the brain.

Results

Spontaneous vasomotion (around 0.1 Hz) can be observed in arterioles in the awake mouse brain

We used *in vivo* two-photon microscopy in awake head-fixed mice to measure spontaneous vasomotion and evoked vascular reactivity to a visual stimulus (functional hyperemia) (Figure 1A–B). Continuous recordings over a 5-minute time course revealed spontaneous vessel dilations and constrictions (in the order of 10–15% diameter change) in individual pial arteries and arterioles in awake mice at ultra-low frequencies (Figure 1C). Fourier transform analyses of these time courses revealed peaks centered around 0.1 Hz (Figure 1C'). Both frequency and amplitude were in line with previous reports of vasomotion in mice (Mateo et al., 2017; He et al., 2018) (Figure 1C'). Spontaneous vasomotion was not regularly observed in veins or venules (Figure 1DD'). No significant differences were observed between the amplitude of the peak at 0.1 Hz between 4–6 months old C57BL/6J (n=5 mice) and 8–10 months old WT littermates of the APP/PS1 mice (n=4 mice), hence data from these mice were pooled in the analyses of this study (and referred to as WT mice). The averaged Fourier plot across WT mice (n=14 arterioles in 8 mice) (for each arteriole ~3 ROIs were averaged) revealed a broad range of ultra-low frequencies (<0.4 Hz) with a distinct peak centered at around 0.1 Hz, but no peaks in the range 0.4–1 Hz (Figure 1E).

Evoked vascular reactivity can be driven at different frequencies of visual stimulation

After recording spontaneous resting vasomotion (Figure 2A–A'), vascular reactivity (*i.e.* functional hyperemia) was evoked in the same vessel in the right visual cortex by presenting a visual stimulation in the left visual field of awake head-fixed mice. Continuous recordings over a 5-minute time course in a single vessel resulted in an increase in vessel diameter change for each period the checkerboard was presented (Figure 2B–C–D). Notably, vascular reactivity could be driven at different frequencies depending on the duration of the flashing checkerboard presentation (Figure 2B–C–D) and the averaged trace revealed a characteristic corresponding hemodynamic response function (Figure 2B'–C'–D'). Likewise, after Fourier transform analyses of a single 5-minute time course, 5 seconds checkerboard ON (followed by 5 seconds grey screen) resulted in a peak at 0.1 Hz (Figure 2B"), 10 seconds checkerboard ON (followed by 10 seconds grey screen) resulted in a peak at 0.05 Hz (Figure 2C"), and 20 seconds checkerboard ON (followed by 20 seconds grey screen), resulted in a peak at <0.05 Hz (Figure 2D") (this was observed in single vessels in 4 mice). Since the most robust response was observed with 10 seconds checkerboard ON (followed by 10 seconds grey screen), this visual stimulation paradigm was used in all subsequent experiments. The averaged hemodynamic response function across WT mice (n=17 arterioles in 9 mice (for each arteriole ~3 ROIs were averaged)) showed that this stimulation paradigm (10 seconds ON/OFF) evoked on average a vessel diameter change of ~7% (Figure

2E). The averaged Fourier plot resulted in a prominent peak at 0.05 Hz (the stimulation frequency) as well as a smaller peak at 0.1 Hz (the vasomotion frequency) (Figure 2F). Notably, evoked reactivity resulted in a 10-fold increase in maximum power at 0.05 Hz (0.13 ± 0.069 1/Hz, n=18 arterioles in 9 mice) and a 5-fold increase in maximum power at 0.1 Hz (0.062 ± 0.042 1/Hz) compared to the maximum power at 0.1 Hz during spontaneous resting-state vasomotion (0.014 ± 0.010 1/Hz, n=14 arterioles in 8 mice).

Paravascular clearance rate is associated with vasomotion in wild-type mice

To measure clearance rates of fluorescent dyes relatively non-invasively (in a physiologically well-preserved closed brain preparation) in awake head-fixed mice, we developed an approach that allowed measuring decay of fluorescent dextrans alongside pial arteries in a reproducible manner (Supplemental Figure 1). Vessels in the neighboring area but distinct from the pial arteries were briefly irradiated (n=26 arterioles and n=22 venules in total). This allowed circulating fluorescent 70 kDa dextran that was intravenously injected at the start of the imaging experiment to extravasate into the brain (Supplemental Video 1). Because of the fast clotting reaction and reperfusion, these transient focal vessel irradiations resulted in the extravasation of single small volumes of fluorescent dextran into the brain tissue, resembling a local bolus dye injection that allowed calculation of clearance rates alongside arterioles (Figure 3A). Small numbers of red blood cells were only occasionally observed to leak out (Supplemental Figure 1). Continuous recordings over 21-minute time courses after vessel irradiations allowed measuring arteriolar oscillations in the ultra-low frequency range (<0.4 Hz) as well as the magnitude of vasomotion (*i.e.* the maximum amplitude at 0.1 Hz) in the artery along which clearance occurred. In WT mice, the maximum sum of the power in the ultra-low frequency range (<0.4 Hz) was not associated with relative dextran intensity at t=18 minutes (Spearman's ρ −0.56, p=0.096), but did show a significant correlation with clearance rates expressed as area under the curve (AUC) (Spearman's ρ −0.67, p=0.039). In contrast, vasomotion (*i.e.* the maximum amplitude at 0.1 Hz) was significantly associated with both relative dextran intensity at t=18 minutes (Spearman's ρ −0.65, p=0.049) and AUC (Spearman's ρ −0.64, p=0.049) (Figure 3B) (n=10 vessels in 8 mice). Visual stimulation resulted in faster clearance rates (Figure 3C), as suggested by a significant difference in relative dextran intensity at t=12 minutes (20.1 ± 10.3 % with visual stimulation (n=11 vessels in 7 mice) vs. 32.2 ± 15.6 % without visual stimulation (n=13 vessels in 9 mice), p=0.038) and t=18 minutes (17.5 ± 9.7 % with vs. 30.0 ± 14.9 % without visual stimulation, p=0.026), but not t=6 minutes (Figure 3C). AUC was reduced by 24%, but this difference did not reach significance (638 ± 226 with visual stimulation (n=11 vessels) vs. 839 ± 341 without (n=13 vessels), p=0.11) (Figure 3E). Visual stimulation during clearance successfully increased the maximum amplitude of the vasoactivity as measured over the whole 21-minute time-course (0.027 ± 0.016 1/Hz at 0.05 Hz with visual stimulation (n=11 vessels) vs. 0.0065 ± 0.0046 1/Hz at 0.1 Hz without visual stimulation (n=12 vessels), p=0.0003) (Figure 3D), and can explain the increased clearance rates observed during visual stimulation.

Importantly, co-injection of i.v. fluorescent nanoparticles with fluorescent dextran in separate C57BL/6J mice independently confirmed unobstructed patterns of paravascular clearance after focal vessel irradiations. Extravasated particles could be observed moving

alongside arterioles in the opposite direction of blood flow (Supplemental Figure 2, Supplemental Video 2), as would be expected in the context of vasomotion-mediated paravascular clearance.

To assess the effect of reduced vasomotion on clearance rates, we used deep (2.5% isoflurane) anesthesia during imaging in a separate set of C57BL/6J mice (Hablitz et al., 2019). As isoflurane acts as a vasodilator, arteriole diameters were found to be significantly increased during isoflurane (n=9 vessels in 4 mice) (32 ± 4 μm) compared to the same vessels imaged awake (21 ± 6 μm, p=0.0003). As expected, isoflurane anesthesia significantly reduced vasomotion and evoked vascular reactivity in arterioles compared to the same arterioles imaged awake. Likewise, clearance rates of extravasated dextran alongside these arterioles were significantly reduced under anesthesia (n=8 vessels in 4 mice) compared to awake (n=9 vessels in 4 mice) (AUC: 1403 ± 453 under isoflurane vs. 881 ± 427 awake, p=0.027 (Supplemental Figure 3).

Spontaneous vasomotion (at 0.1 Hz) and paravascular clearance are not altered in 8–10 months old APP/PS1 mice

It has been proposed that the accumulation of Aβ in the walls of cerebral vessels as observed in patients with CAA is due to impaired paravascular drainage of solutes, including Aβ (Arbel-Ornath et al., 2013; Wojtas et al., 2017). Impaired clearance may be due to reduced vascular compliance, as it was previously demonstrated with fMRI that patients with CAA show impaired vascular reactivity in the visual cortex after visual stimulation (Dumas et al., 2012; Peca et al., 2013). To assess the effect of CAA on paravascular clearance, 8–10 months old Tg APP/PS1 mice – that exhibit mild CAA burden in pial arteries (Figure 4A) – were compared to WT mice. Interestingly, the averaged Fourier plots of resting-state activity recorded continuously over 5 minutes (with the screen off) in arterioles in head-fixed awake Tg animals (Figure 4B) revealed that spontaneous arteriolar oscillations in the ultra-low frequency range (<0.4 Hz) including spontaneous vasomotion (*i.e.* the peak at 0.1 Hz) were preserved at this age (Figure 4C). Compared to WT mice there was no significant difference between the maximum sum of the power in the ultra-low frequency range (<0.4 Hz) (0.67 ± 0.61 1/Hz in Tg (n=13 vessels in 4 mice) vs. 0.85 ± 0.44 1/Hz in WT mice (n=14 vessels in 8 mice), p=0.39) or the magnitude of vasomotion (maximum amplitude at 0.1 Hz was 0.0094 ± 0.0083 1/Hz in Tg vs. 0.014 ± 0.010 1/Hz in WT mice, p=0.29) (Figure 4D). Likewise, clearance in Tg mice was not notably different from clearance in WT mice under resting-state conditions (Figure 4E), as quantified by relative dextran intensity at t=6, 12, or 18 minutes and AUC (908 ± 510 in Tg vs. 839 ± 341 in WT mice, p=0.70) (Figure 4F). Vasomotion measured during the 21-minute time course of dextran clearance also did not differ substantially between Tg (maximum amplitude at 0.1 Hz was 0.005 ± 0.005 1/Hz (n=11 vessels in 4 mice)) and WT mice (maximum amplitude at 0.1 Hz was 0.007 ± 0.005 1/Hz at 0.1 Hz (n=12 vessels in 8 mice), p=0.49), nor did the maximum sum of the power in the ultra-low frequency range (<0.4 Hz) (0.45 ± 0.35 1/Hz in Tg vs. 0.55 ± 0.35 1/Hz in WT mice, p=0.53). Finally, within Tg mice, CAA burden was calculated for each arteriole alongside which clearance was measured, which did not reveal an association with clearance rates as expressed as AUC (Spearman's ρ −0.15, p=0.67) (data not shown).

A subset of mice was re-imaged again ~4–5 months later, when they were around 14 months old. At that age, spontaneous arteriolar oscillations in the ultra-low frequency range as recorded over 5 minutes tended to be reduced in head-fixed awake 14 months old Tg mice (n=11 vessels in 8 mice) compared to 14 months old WT mice (n=11 vessels in 8 mice), and no prominent peaks at 0.1 Hz were observed (Supplemental Figure 4), suggesting reduced spontaneous vasomotion in older APP/PS1 mice.

Evoked vascular reactivity and paravascular clearance rates are reduced during visual stimulation in 8–10 months old APP/PS1 mice

In contrast, evoked vascular reactivity recorded over 5 minutes was significantly impaired in 8–10 months old Tg mice compared to WT, as suggested by the averaged hemodynamic response functions to the checkerboard stimulation (Figure 5A), and the quantification of the maximum amplitude of the power at 0.05 Hz after Fourier transform (0.043 ± 0.034 1/Hz (n=22 vessels in 5 Tg mice) vs. 0.13 ± 0.069 1/Hz (n=18 vessels in 9 WT mice), p<0.0001) (Figure 5B). Evoked vascular reactivity measured during the 21-minute time course of dextran clearance was similarly impaired in Tg (0.015 ± 0.012 1/Hz (n=13 vessels in 5 mice)) compared to WT mice (0.027 ± 0.016 1/Hz (n=11 vessels in 7 mice), p=0.033) (Figure 5D). Likewise, clearance rates were significantly slower in Tg mice compared to WT (Figure 5C), as quantified by relative dextran intensity at t=6 (51.6 ± 29.8 % in Tg (n=13 vessels) vs. 29.1 ± 14.7 % in WT mice (n=11 vessels), p=0.033), t=12 (38.2 ± 20.8 % in Tg vs. 20.1 ± 10.3 % in WT mice, p=0.016), and t=18 minutes (35.3 ± 19.2 % in Tg vs. 17.5 ± 9.7 % in WT mice, p=0.011) and an increase in AUC of 59% (1017 ± 433 in Tg vs. 638 ± 226 in WT mice, p=0.016) (Figure 4E). Importantly, across WT and Tg animals, the magnitude of the evoked reactivity during clearance significantly correlated with clearance rates expressed by AUC, at the stimulation frequency (*i.e.* the maximum amplitude at 0.05 Hz, Spearman's ρ −0.59, p=0.0041) (Figure 5F) and even more strongly at the vasomotion frequency (*i.e.* the maximum amplitude at 0.1 Hz, Spearman's ρ −0.64, p<0.001).

Since vessel irradiations may affect Tg animals differently compared to WT, we sought to confirm our findings with an independent model system. In a separate cohort of 8–10 months old Tg APP/PS1 mice and their WT littermates, 50 μL unconjugated fluorescein was intravenously injected during imaging. Given that unconjugated fluorescein selectively crosses the blood-brain barrier and is rapidly cleared from the circulation, paravascular clearance rates of extravasated fluorescein could be measured after each injection without the need for vessel irradiations. Importantly, clearance rates were slower in Tg mice (n=9 vessels in 5 mice) compared to WT (n=5 vessels in 3 mice) (AUC: 1259 ± 319 in Tg vs. 909 ± 265 in WT mice, p=0.060), during visual stimulation (Supplemental Figure 5).

Reduced vascular reactivity in APP/PS1 mice is not driven by altered neuronal responses

To determine whether the observed impaired evoked vascular reactivity was driven by differences in neuronal activation between Tg APP/PS1 mice and their WT littermates, a separate cohort of 8–10 months old mice was included that underwent intra-cortical injections with the Calcium (Ca^{2+}) indicator GCaMP6s targeted to neurons to record neuronal responses to the same visual stimulus (Figure 6A–B). Neurons were classified based on their response to the visual stimulus (10 seconds checkerboard ON, 10 seconds

OFF, see methods) (Figure 6C–D). No significant differences were observed in the average percentage of ON responders (p=0.67), OFF responders (p=0.65), NON responders (p=0.38), or Mixed responders (p=0.64) between WT (total number of 200 neurons in 6 mice) and Tg mice (total number of 178 neurons in 5 mice) (Figure 6E). Also, no difference was observed between the amplitude of the fluorescent signal change in ON responders, between WT (72 ON responders) and Tg mice (55 ON responders) (Figure 6F). Yet, evoked vascular reactivity was significantly impaired in this cohort of animals, as recorded at the same resolution and frame-rate as the neurons (Figure 6G). These results suggest that impaired clearance in mice with CAA is driven by vascular rather than neuronal impairments.

To assess the focality of the hemodynamic responses and to verify whether the neuronal and vascular responses were indeed related to visual activation, we recorded neuronal and vascular responses to the same visual simulation paradigm in somatosensory cortex in 2 C57BL/6J mice (Star Methods). Importantly, virtually no neuronal or vascular responses were observed outside the visual cortex, supporting the focality of the hemodynamic response evoked by visual stimuli (Supplemental Figure 6).

Reduced vascular reactivity in APP/PS1 mice is not associated with local CAA burden, but with loss of vascular smooth muscle cells

One possible mechanism for CAA-related impairment in vascular reactivity is increased arterial stiffness due to local vascular Aβ deposits. To evaluate this notion, we quantified CAA burden for different vessel segments on maximum intensity projections of the Methoxy-X04 channel in 8–10 months old Tg mice that underwent visual stimulation (Figure 7A–B). No significant correlation was found for CAA burden and evoked vascular reactivity per vessel segment (Spearman's ρ −0.098, p=0.58, n=35 vessel segments in 5 mice) (Figure 7C). These results remained unchanged when multiple ROIs were averaged per vessel. This observation suggests that local CAA is not directly responsible for impaired vessel function. A likely alternative explanation for vessel dysfunction could be degeneration of vascular SMCs, a known pathological manifestation of CAA (Vonsattel et al., 1991; Zipfel et al., 2009). We quantified SMC density with *ex vivo* immunohistochemistry in brain sections of WT (n=8 mice) and Tg (n=6 mice) that underwent *in vivo* two-photon microscopy and were on average 18 months old at time of euthanasia. SMC density was reduced in Tg (5.5 ± 2.8 %, n=28 vessels) compared to WT mice (7.1 ± 4.1 %, n=34 vessels, p=0.076) (Figure 7D–E). Within the transgenic animals three vessels did not exhibit any CAA. Excluding these vessels (with an average SMC density of 10.1 ± 4.5 % (n=3 vessels)) from the analysis resulted in a significant difference in SMC density between Tg and WT mice (p=0.016) (Figure 7F). These findings suggest that SMC degeneration in CAA-affected vessels may be responsible for the observed impaired vascular reactivity and paravascular clearance deficits.

APP/PS1 mice exhibit progressive loss of vascular smooth muscle cells, independent of local CAA burden

Finally, to demonstrate loss of SMCs *in vivo* in the APP/PS1 mouse model, we crossed APP/PS1 mice with smMHC(Myh11)/Cre/eGFP (SMC/Cre/eGFP) mice (that express green

fluorescent protein in vascular SMCs) to perform longitudinal (*i.e.* monthly) *in vivo* imaging of SMCs in a separate cohort (Star Methods). Relative SMC number did not change over a period of approximately 10 months in (n=2) WT littermates (mouse 1: −0.0042 ± 0.0032, n=16 ROIs, p=0.23; mouse 2: −0.011 ± 0.0058, n=23 ROIs, p=0.12). However, relative SMC number decreased over the same period in (n=2) Tg APP/PS1 mice (mouse 1: −0.053 ± 0.016, n=33 ROIs, p=0.043; mouse 2: −0.050 ± 0.0050, n=27 ROIs, p=0.0006). Within the Tg mice, the observed loss of SMCs tracked very closely with overall increase in CAA burden (mouse 1: 0.053 ± 0.015, n=33 ROIs, p=0.040; mouse 2: 0.046 ± 0.0054, n=29 ROIs, p=0.0011), but within each ROI at the level of individual vessel segments the rate of SMC loss was not associated with the rate of CAA progression (Pearson's r 0.088, p=0.50) (Supplemental Figure 7). These findings confirm our *ex vivo* immunohistochemistry observations and lend further support to the idea that loss of vascular SMCs rather than local CAA burden *per se* is responsible for deficits in vessel physiology and paravascular clearance in APP/PS1 mice.

Discussion

The findings from this study suggest that paravascular clearance of solutes from the brain in awake mice are driven by ultra-slow arteriolar SMC oscillations. The rate of decay of extravasated fluorescent dextrans alongside arterioles correlated with the amplitude of local vasomotion, quantified as the maximum vasodilation at 0.1 Hz. When the amplitude of vasomotion was physiologically increased by means of functional hyperemia, clearance rates also increased in WT mice. Mice with vascular Aβ depositions showed impaired vasodilation during functional hyperemia, which was associated with slower clearance rates. Neuronal calcium imaging using the same visual stimulation paradigm suggested that these observed differences were not driven by altered neuronal responses. Our data suggest that CAA is accompanied by loss of SMCs that results in reduced vessel reactivity and impaired paravascular clearance of solutes. These findings have important implications for therapeutic options directed towards the removal of Aβ from the brain.

Drainage of soluble waste products, including Aβ, from the brain is important for maintenance of brain health (Xie et al., 2013; Kress et al., 2014; Benveniste et al., 2019). Impaired clearance has been implicated in healthy aging (Kress et al., 2014), and age-related brain diseases such as AD and CAA (Weller et al., 2000; Weller et al., 2009; Peng et al., 2016). An important unanswered question in the field is what the precise underlying mechanisms are and contributing components of clearance. Although there is still controversy regarding both the directionality of flow and whether solutes in ISF move through the tissue by convection or diffusion (Bakker et al., 2016; Smith et al., 2017), there is consensus that clearance out of the brain happens alongside vessels (Benveniste et al., 2019). Specifically, accumulating evidence suggests intra-mural drainage along basement membranes of SMCs within the walls of arteries (Carare et al., 2008; Albargothy et al., 2018). We purposefully used the term 'paravascular' throughout this paper, since the resolution of *in vivo* two-photon microscopy is not sufficient to resolve the intra-mural peri-arterial drainage pathway itself. As such, we experimentally measured fluorescent decay within ROIs alongside arteries (*i.e.* paravascular), under the assumption that paravascular fluorescent decay is directly related to peri-arterial clearance (*i.e.* perivascular).

To date the exact driving force responsible for intra-mural peri-arterial clearance remains elusive. Previous work has suggested pulsatile blood flow as a potential motive force, based on mathematical modeling (Schley et al., 2006; Wang et al., 2011) and experimental studies in anesthetized rodents that relied on surgical and pharmacological interventions to respectively reduce or increase arterial pulsations (Iliff et al., 2013; Mestre et al., 2018). More recently however, two modeling studies suggested that arterial pulsations alone are likely to be too weak to drive peri-arterial clearance (Asgari et al., 2016; Diem et al., 2017). It was suggested that other forces would be necessary to produce the right pressure gradient required to push fluid through peri-arterial pathways, and that the rhythmic spontaneous contractions of vascular SMCs (*i.e.* vasomotion), which generate much shorter wavelengths (in the order of millimeters) compared to arterial pulsations (in the order of meters) (Aldea et al., 2019), would be likely candidates (Diem et al., 2017). Our observation of nanoparticles traveling alongside arteries in the opposite direction of blood flow fits well with vasomotion-derived intra-mural peri-arterial clearance as described recently (Aldea et al., 2019). It is not unlikely in retrospect that previous studies that experimentally changed arterial pulsations to assess the effect on clearance rates, also interfered with normal vasomotion properties, which could explain their findings (Iliff et al., 2013; Arbel-Ornath et al., 2013; Mestre et al., 2018). That said, physiologically increasing the vasomotion amplitude by means of functional hyperemia (in our study) may also have triggered an increase in arterial pulsations. Moreover, we cannot exclude aliasing from >1 Hz frequency oscillations that may have been present but were not captured in our recordings. As such, the potential additive contribution of higher frequency pulsations on clearance rates cannot be ruled out. Similarly, we cannot rule out a potential contribution of movement-induced vasodilations (triggered by locomotion of the mouse on the treadmill) to the observations in the ultra-low frequency range (Winder et al., 2017). To limit this potential effect, we discarded measurements contaminated by extensive locomotion. Moreover, although movement-induced vasodilatons were occasionally observed, the overall contribution to the vasomotion signal seemed to be modest, given the low variation of the observed amplitude at 0.1 Hz on average (Figure 1E). Another potential confounder is the impact of blood pressure and blood gases, for which we did not obtain values in our experiments but may affect cerebral blood flow globally. However, the finding that the hemodynamic responses were largely restricted to the visual cortex diminishes the concern that changes in these systemic variables may have influenced our observations.

In our study, we performed the first direct experimental test of the hypothesis whether clearance is driven by a heretofore unaddressed potential motive force generated by ultra-slow SMC-derived arteriolar contractions and dilations; vasomotion. Spontaneous vasomotion is thought to occur relatively independent from heart beat pulsations or the respiratory cycle and has been observed in isolated arterioles from rodents (Osol et al., 1988; Filosa et al., 2004) and in the absence of neuronal activity (Brown et al., 2002; Winder et al., 2017). Early experimental studies have demonstrated that the rhythmic low frequency contractile activity of arteries is driven by membrane calcium and potassium conductance and can be modulated (*e.g.* with nitric oxide, anesthesia) (Osol et al., 1988; Dirnagl et al., 1993). Evidence that vasomotion occurs in humans comes from the observation of ultra-slow hemodynamic oscillations centered at around ~0.1 Hz in pial surface vessels during brain-

exposed surgical interventions (Rayshubskiy et al., 2014; Noordmans et al., 2018). More recently, it has been suggested that spontaneous vasomotion is the underlying principle of the resting-state blood-oxygen-level dependent (BOLD) signal in functional magnetic resonance imaging (MRI) studies in rodents (Mateo et al., 2017; He et al., 2018). Here we directly linked vasomotion to paravascular clearance *in vivo* and found that increasing the vasomotion amplitude also resulted in increased clearance. Likewise, reducing vasomotion under deep isoflurane anesthesia resulted in reduced clearance. Interestingly, although vascular reactivity was evoked at a lower frequency (0.05 Hz) than the intrinsic vasomotion frequency (0.1 Hz), peaks at both 0.05 Hz and 0.1 Hz were frequently observed on the resulting Fourier plots. Although the maximum amplitude at 0.05 Hz significantly correlated with clearance rates, the amplitude at 0.1 Hz revealed a stronger association, suggesting that the 0.1 Hz frequency may be the most dominant motive force. We did not directly assess whether increasing the vasomotion frequency (>0.2 Hz) rather than the amplitude may also influence clearance rates. This would be an interesting topic for future studies, although there may be limits to what can be driven physiologically by functional hyperemia (Figure 2). Other more direct approaches to increase or decrease vasomotion, such as optogenetics, could be powerful means to achieve this in the future, although this method presents its own limitations.

Our findings of impaired paravascular clearance in mice with CAA are in line with previous observations in lightly anesthetized animals (Arbel-Ornath et al., 2013; Peng et al., 2016). Here we show that impaired evoked vascular reactivity in awake mice with CAA is directly related to reduced clearance of fluorescent dextran. Whether our findings also apply to clearance of soluble Aβ remains to be assessed, since we did not directly measure clearance of Aβ. Such an experiment would have required injections of fluorescently labeled Aβ species in awake mice, which is challenging for several reasons (as discussed below) and could be considered a limitation of our study. That said, our findings have implications for understanding drainage of Aβ from the brain. Since vascular Aβ depositions in patients with CAA (Vinters et al., 1987) and in Tg mice that overproduce Aβ (Jäkel et al., 2017) are predominantly found in the walls of cortical arterioles and leptomeningeal arteries, Aβ clearance appears likely to occur alongside arteries rather than veins. More specifically, since Aβ deposits within vascular SMC basement membranes of the tunica media in patients with CAA, this compartment has been implicated as a major clearance pathway of soluble Aβ (Weller et al., 2003; Albargothy et al., 2018). Consequently, SMC dysfunction could be a likely contributor to impaired clearance in CAA. SMC degeneration is a prominent feature of severe CAA and has been extensively described in humans (*e.g.* Vonsattel et al., 1991; Weller et al., 2003; Love et al., 2014; Charidimou et al., 2017), and in Tg2576 mice (Christie et al., 2001; Zipfel et al., 2009). Our longitudinal observations in APP/PS1 mice are in line with these previous findings and furthermore suggest that although SMC loss is associated with a regional increase in CAA burden, they do not track together at the single-vessel segment level. This may explain the lack of a correlation between local CAA burden and evoked vascular reactivity within Tg mice, although this was previously observed in older anesthetized hAPPJ20 mice (Kimbrough et al., 2015). A possible explanation for this discrepancy is the presence of oligomeric Aβ, not labeled by Methoxy-X04, which could be responsible for local SMC injury in the absence of visible vascular Aβ depositions (Davis et

al., 1999; Blaise et al., 2012). Other pathophysiological pathways including reactive oxygen species and endothelial dysfunction may play a role as well (Iadecola et al., 1999; Park et al., 2013). Patients with CAA exhibit impaired evoked vascular reactivity in response to a flashing checkerboard as measured with BOLD fMRI in the visual cortex (Dumas et al., 2012; Peca et al., 2013; Van Opstal et al., 2017), in line with our findings in individual vessels in mice with CAA using a similar visual stimulation paradigm. Interestingly, in patients with a hereditary form of the disease (*i.e.* Dutch-type CAA) the hemodynamic response was already impaired in young asymptomatic mutation-carriers (Van Opstal et al., 2017). These findings suggest that SMC-related reduced vascular reactivity may be an early feature of the disease, potentially resulting in further impaired paravascular clearance of Aβ. It is further notable that CAA in adult APP/PS1 mice is relatively mild relative to diagnosed human CAA pathology, implying that vasomotion in these mice (preserved in resting 8–10-month-old Tg mice and impaired only in the setting of visual stimulation) may underestimate the extent of vasomotion impairment in advanced human CAA. Our findings in 14-month-old mice suggest that resting vasomotion is indeed affected in older mice with CAA, likely due to a progressive loss of SMCs. The effect of aging on vascular function and clearance will be an interesting topic for future studies as is the effect of more severe CAA on vascular function, which may be more reliably addressed in other mouse models (Park et al., 2014). So far, it has proven challenging to detect vasomotion in humans non-invasively utilizing fMRI techniques, but this would be an important technical advancement to address these questions in patients with small vessel disease.

The observation of comparable neuronal responses to the visual stimulation between WT and Tg mice suggests that reduced vascular function rather than neuronal activity is responsible for the impaired evoked vascular reactivity in mice with CAA, which is in line with previous findings (Niwa et al., 2000). An alternative explanation could be impairments in neurovascular coupling, driven by potential functional changes in astrocytes or astrocytic endfeet in mice with CAA (Kimbrough et al., 2015; Kelly et al., 2018). Whether altered astrocytic function may have played a role was not assessed and is an important topic for future studies. It should also be noted that other means of vascular clearance, such as transport across the blood-brain barrier (Sweeney et al., 2018), are likely impaired in Tg compared to WT mice and may have played a role in the observed differences reported here.

To measure clearance in awake mice, we used focal laser irradiations to allow small volumes of circulating dextran to extravasate into the tissue. Previous studies that assessed clearance rates *in vivo* in rodents required invasive surgical techniques to deliver fluorescent contrast agents directly into the brain (Arbel-Ornath et al., 2013; Kress et al., 2014; Peng et al., 2016; Albargothy et al., 2017). Two disadvantages of these approaches are that they require general anesthesia and direct access to the cortical parenchyma or CSF compartments such as the cisterna magna to deliver dyes, which influence systemic and brain physiology in several ways and likely affect clearance rates as well. We found that deep isoflurane anesthesia significantly impacted clearance rates, which is in line with previous finding of reduced influx of tracers into the CSF under isoflurane anesthesia (Hablitz et al., 2019). In addition, we observed that isoflurane strongly reduced vasomotion, which is a likely explanation for these findings. That said, isoflurane has several mechanisms of action, and it cannot be firmly concluded that reduced vasomotion is the only reason for the observed

slower clearance rates. In general, when comparing findings from different experimental studies it is important to consider the anesthetic regimen used, as it may differentially influence vascular properties and paravascular clearance *in vivo* (Hablitz et al., 2019). To the best of our knowledge, our study is the first to relatively non-invasively study paravascular clearance in awake mice in a physiologically well-maintained cerebral environment. Yet our method presents its own limitations. Although the laser irradiation approach of neighboring vessels was reproducible and generally resulted in the extravasation of only small volumes of dextran, the exact amount of dextran delivery could not be controlled for *a priori*. Moreover, edema may have formed in the brain tissue in response to the irradiation, which we did not control for and may have influenced clearance rates. However, there is no reason to believe the severity of potential edema formation to be different between conditions (*e.g.* screen off vs. checkerboard) and as such the observed differences are not likely due to this potential confound. To reduce variability, irradiations that resulted in excessive leakage or re-leakage were excluded from further analysis. Moreover, the approach was found to be comparable between WT and Tg (Supplemental Figure 1), which allowed us to reliably measure differences in clearance rates between these two groups. Importantly, we independently confirmed our findings with another fluorescent tracer delivery method that did not rely on vessel irradiations in a separate set of APP/PS1 mice (Supplemental Figure 5). Moreover, co-injection of nanoparticles with dextran in C57BL/6J mice validated our laser irradiation approach as unobstructed paravascular clearance was observed to happen alongside arterioles in cadence with vasomotion. Even though these observations suggest that this approach enables to reliably track paravascular clearance pathways *in vivo*, we should keep in mind that any given fluorescent dye delivery method in mice – whether through cisterna magna injections or vessel irradiations – inherently results in an imperfect representation of normally-occurring clearance of solutes from ISF. By trying to limit some of the non-physiological variables related to anesthesia and pressure-injections we aimed to create a more representative model system to study the role of vasomotion on clearance in awake animals, but this system likely needs further refinement in future studies.

In conclusion, our experimental findings in awake mice support the recently suggested possibility that SMC-derived slow arteriolar fluctuations are a motive force of paravascular drainage (Diem et al., 2017; Aldea et al., 2019). Our data raise the possibility of increased vascular activity as a therapeutic option for the removal of soluble Aβ from the brain. Moreover, early intervention targeted to preserving SMCs may be a promising avenue for the prevention of brain diseases including AD and CAA.

STAR Methods text

Lead Contact and Materials Availability

Further information and requests for resources and reagents should be directed to and will be fulfilled by the Lead Contact, Susanne van Veluw (svanveluw@mgh.harvard.edu). This study did not generate new unique reagents.

Experimental Model and Subject Details

Mice—Three-to-five months old male C57BL/6J mice (Jackson laboratories) and seven-to-nine months old male and female transgenic (Tg) APPswe/PSEN1dE9 (APP/PS1) mice and their wild-type (WT) littermates were used for the experiments described in this study. The APP/PS1 mouse model expresses the human mutant amyloid precursor protein (APP) gene containing the Swedish mutation K594N/M595L and the human presenilin 1 gene lacking exon 9, both under the control of the PrP promotor (Jankowsky et al., 2001). In this model, parenchymal Aβ plaques start to deposit around five months of age and around the same time CAA appears in the form of vascular Aβ deposits on pial arteries and arterioles, increasingly with age (Garcia-Alloza et al., 2006). Since sex does not influence CAA progression in this model (Garcia-Alloza et al., 2006), both sexes were used in this study. APP/PS1 mice were purchased from The Jackson Laboratory and bred in our animal facility to produce offspring. Mice were housed with up to four individuals in one cage and alone after surgical procedures on a 12-hour light/dark cycle and food and water was provided *ad libitum*. All animal procedures were performed with the approval of the Massachusetts General Hospital Animal Care and Use Committee and in compliance with the National Institutes of Health Guide for the Care and Use of Laboratory Animals.

Method Details

Surgical procedures—Cranial window surgery was performed as described previously, with minor modifications (Arbel-Ornath et al., 2013; Kuchibhotla et al., 2014). Mice were anesthetized with isoflurane (5% inhalation, mixed with pure O_2) and placed in a stereotactic frame, after which isoflurane was maintained at 1.5–2% throughout the procedure. A craniotomy (measuring 3 mm in diameter) was performed exposing the right visual cortex (the lower left corner of the window was positioned at 1 mm caudal, 1.5 mm lateral from lambda). A cover glass measuring 5 mm in diameter was placed over the brain and secured with a mixture of dental cement and Krazy Glue. A custom-made stainless-steel headpost (Ponoko) was attached to the skull using C & B Metabond (Parkell), allowing the mice to be head-fixed while imaged awake. A separate cohort of Tg APP/PS1 mice and their WT littermates received a single intra-cortical injection of the genetically encoded calcium indicator GCaMP6s (which has greater sensitivity compared to the faster responding GCaMP6f (Chen et al., 2013)) targeted to neurons (AAV1.Syn.GCaMP6s.WPRE.SV40, UPenn Vector core) after craniotomy. A total volume of 2 μl of viral vector was injected through a 33-gauge needle attached to a Hamilton syringe at 0.6 mm depth below the pial surface at a flow-rate of 150 nL/minute using a stereotactic injector (Harvard apparatus). Mice received a single subcutaneous injection of buprenorphine (0.05 mg/kg) and Tylenol (300 mg/mL) in their drinking water for up to three days post-surgery and were allowed to recover for at least four weeks before they were imaged. In addition, craniotomies (measuring 5 mm in diameter) over the somatosensory cortex and bilateral intra-cortical injections of GCaMP6s were performed in 2 C57BL/6J mice.

Two-photon microscopy set-up—Mice were imaged using a FluoView FV1000MPE two-photon laser-scanning system (Olympus) mounted on a BX61WI microscope (Olympus), equipped with a long working distance 25x (numerical aperture = 1.05) dipping water immersion objective (Olympus). A Mai Tai® DeepSee^{tm} Ti:Sapphire mode-locked

laser (Spectra-Physics) generated two-photon excitation at 800 nm (to record vascular activity) or 900 nm (to record neuronal activity). External detectors containing three photomultiplier tubes (PMTs, Hamamatsu) collected emitted light in the range of 420–460 nm (blue), 495–540 nm (green), and 575–630 nm (red). PMT settings were kept constant for each experiment, but laser power was adjusted as needed. Mice were imaged awake during daytime and allowed to move freely on a circular treadmill while being secured in place by fastening their headposts in a stereotactic frame. Mice were visually monitored throughout the duration of the imaging session (which lasted on average 2 hours), or imaging was stopped when they became inattentive. To evoke local neuronal and vascular responses to a visual stimulus, a 19" LCD monitor (Acer) was placed in the left visual field of the mouse at a distance of approximately 20 cm and at an angle of 60 degrees. The visual stimulus was operated through Matlab (version R2016a; MathWorks) and consisted of a flashing checkerboard pattern (2 × 2 cm^2 white and black squares alternated at a frequency of 5 Hz) that was presented for a length of time (*e.g.* 10 seconds ON) followed by a grey screen for the same length (*e.g.* 10 seconds OFF), repeatedly for 5 minutes total. A red dot presented in the center of the screen served as fixation point. To avoid light contamination, the emission path was shielded with a custom-made black fabric mask attached to the objective and frame with light-tight tape. Spontaneous activity recordings were acquired with the screen off.

Vascular and neuronal activity recordings—The day prior to imaging Tg APP/PS1 mice were intraperitoneally injected with 300 μL Methoxy-X04 solution (Glixx lab) (~5 mg/kg dissolved in 3% Cremophor® EL (Sigma) and phosphate-buffered saline (PBS)) to visualize Aβ depositions *in vivo*. WT mice were also injected to verify their genotyping. Right before imaging mice were briefly anesthetized with isoflurane and retro-orbitally injected with 200 μL 70 kDa fluorescein or Texas Red dextran (12.5 mg/mL; Invitrogen) to provide a fluorescent angiogram *in vivo*. Z-stacks were acquired at a speed of 4 μs/pixel, a pixel resolution of 1 μm^2 (512×512), and a step size of 5 μm at 1x magnification. Spontaneous vasomotion was recorded in pial arteries and first-order arteriolar branches (which were identified based on their morphology, direction, and velocity of blood flow) continuously over 5 minutes at a speed of 2 μs/pixel, a pixel resolution of 1 μm^2 (256×256), and a frame-rate of ~2 Hz (a total number of 700 frames was acquired) at 2x magnification with the screen off. Evoked vascular reactivity to the visual stimulus was recorded over 5 minutes at the same speed, resolution, frame-rate, and magnification. Spontaneous neuronal activity was recorded continuously over 5 minutes at a speed of 2 μs/pixel, a pixel resolution of 2 μm^2 (128×128), and a frame-rate of ~5 Hz (a total number of 1600 frames was acquired) at 2x magnification with the screen off. Evoked neuronal activity to the visual stimulus was recorded over 5 minutes at the same speed, resolution, frame-rate, and magnification. Per mouse on average 1–2 fields of view (FOVs) were obtained. Additional recordings were obtained to measure evoked vascular reactivity at 128×128 resolution and higher frame-rate in this second cohort of mice. A subset of mice was imaged again ~4–5 months later under the same conditions to assess the effect of aging and increased CAA severity on spontaneous vasomotion and evoked vascular reactivity. Neuronal and vascular recordings in the 2 C57BL/6J mice with windows over somatosensory cortex were obtained in the same fashion.

Paravascular clearance recordings—To non-invasively measure clearance alongside arteries in awake animals, vessels (n=32 arterioles and n=22 venules) were briefly irradiated to allow fluorescent dextran to enter the parenchyma. Vessel irradiation was achieved at 800 nm excitation wavelength by focusing the laser at maximum power (100%, which roughly equals 234 mW as measured at the front lens of the objective, compared to 25 mW at 10% 'normal' laser power) for 20 seconds per attempt in bidirectional scanning mode on a small segment of the targeted vessel at 6x magnification, and was immediately stopped when dextran was observed to leak out of the vessel. Due to the fast clotting reaction (within seconds) a typical successful focal vessel irradiation resulted in the extravasation of a single small volume (or bolus) of fluorescent dextran. Paravascular clearance of extravasated dextran was measured alongside separate neighboring arteries continuously over a period of 21 minutes at a speed of 2 μs/pixel, a pixel resolution of 1 μm^2 (256×256), and a frame-rate of ~2 Hz (a total number of 3000 frames were acquired) at 2x magnification. During clearance either the visual stimulus was presented on the screen or the screen was off. Mice underwent a second imaging session on average 1–2 weeks later. Any measurement in which re-leakage from the irradiated vessel was observed was excluded from further analyses (n=2 arterioles in WT and n=4 arterioles in Tg mice). Importantly, for all clearance measurements reported in this study, both the distance between the irradiated vessel and the ROI in which clearance was measured as well as the diameter of the arteriole alongside which clearance was measured were comparable between conditions and WT and Tg mice. Moreover, the effect of the vessel irradiation approach was comparable between conditions and WT and Tg mice. No differences were observed for time to leak, time to reperfusion of the irradiated vessel, extravasated dextran volume, and occurrence of leakage of small numbers of red blood cells (Supplemental Figure 1).

Isoflurane—To assess the effect of deep isoflurane anesthesia on vasomotion and clearance rates, a separate set of C57BL/6J mice (n=4) with chronic cranial windows implanted over the right visual cortex were imaged both awake and anesthetized (5% isoflurane induced, 2.5% maintained throughout imaging) within the same imaging session. Fluorescein dextran was injected once prior to imaging. Mice were randomly assigned to be first imaged awake (as described above) or under isoflurane anesthesia. During anesthesia, the mice were placed in a stereotactic frame and a heating pad was placed on top of them to keep them at body temperature, while all other settings were kept similar compared to awake imaging. When switching from awake imaging to anesthetized or *vice versa*, enough time was allotted to ensure mice were fully awake or anesthetized (*e.g.* no response to foot pinch) respectively. During all clearance measurements, the screen was kept off.

Nanoparticles—To provide an independent way to assess paravascular clearance more directly, blue fluorescent (~20 nm) nanoparticles (150 μl; Ocean Nanotech LLC) were retro-orbitally co-injected with 70 kDa Texas Red dextran (150 μl) prior to imaging in a separate set of C57BL/6J mice (n=3) with chronic cranial windows implanted over the right visual cortex. After focal irradiations of nearby vessels, 5-minute time courses were recorded at a speed of 2μs/pixel, a pixel resolution of 1 μm^2 (256×256) and a frame-rate of ~2 Hz (a total number of 700 frames were recorded) at 2x magnification with the screen off. Moreover, high-frame rate 30-second time courses were recorded in bidirectional scanning mode at a

speed of 0.244ms/line and a frame-rate of ~15 Hz (a total number of 450 frames were recorded) at 6x magnification.

Unconjugated fluorescein—To provide an independent way to assess paravascular clearance without the need for vessel irradiations, ~3.5 mg/mL unconjugated fluorescein (50 μL; Sigma-Aldrich) in PBS was retro-orbitally injected during imaging in a separate set of 8–10 months old Tg APP/PS1 mice (n=5) and their WT littermate controls (n=3) with chronic cranial windows implanted over the right visual cortex. Because of fluorescein's higher risk of photobleaching, after injections a total of 8 Z-stacks were recorded over a 21-minute time-period, with 3-minute intervals, at a speed of 4μs/pixel, a pixel resolution of 1 μm^2 (512×512) at 2x magnification.

Longitudinal imaging of vascular smooth muscle cells—To assess the loss of smooth muscle cells (SMCs) in the context of CAA, APPswe/PSEN1dE9 (APP/PS1) mice were crossed with smMHC(Myh11)/Cre/eGFP (SMC/Cre/eGFP) mice (purchased from the Jackson Laboratory and bred in our animal facility to produce offspring). Both Tg and WT littermates were imaged once-a-month anesthetized (5% inhalation, 1.5–2% throughout the imaging session) with *in vivo* two-photon microscopy through chronic cranial windows over somatosensory cortex. The same vessels were imaged longitudinally. Each arteriole was divided into ROIs of similar size capturing on average 10 individual SMCs at the first imaging session. These ROIs were placed at the same position for each subsequent imaging session. Relative SMC number was determined for each ROI as a fraction of the SMC number counted in that ROI in the first imaging session. CAA burden was quantified for each ROI as the fraction CAA positive pixels. SMC loss rate and CAA progression rate were determined as the slope of each variable.

Ex vivo tissue processing—Mice were euthanized by CO_2 asphyxiation and transcardially perfused with PBS. Brains were rapidly extracted, and hemispheres were separated by a single midsagittal cut. The left hemisphere was stored in 4% paraformaldehyde + 15% glycerol (PBS) solution, but not further processed for this study. The right hemisphere (over which the craniotomy was performed) was fixed for 24 hours in 4% paraformaldehyde + 15% glycerol (PBS) solution, then cryoprotected, frozen at −20 °C, and cut in 20 μm-thick sections in axial orientation using a cryostat. Sections were blocked in 5% normal goat serum, then incubated overnight at 4°C with anti-SMC actin (1:250; Dako) to assess vascular SMC morphology and density. Goat anti-mouse Alexa Fluor 488 (1:500; Invitrogen) served as the secondary antibody. Dylight 594-conjugated Tomato lectin (1:500; Fisher scientific) was applied to the sections to distinguish vessels. CAA was visualized by Methoxy-X04, which was re-injected intraperitoneally in Tg mice one day prior to euthanasia. Negative controls were included by omitting the primary antibody and the lectin. Per mouse, 4–5 brain sections at the level of the cranial window were imaged on a Zeiss fluorescent microscope, using a 20x objective. Z-stack images (2 μm step size) were taken of areas with SMC-positive pial surface arterioles for each channel, keeping exposure time constant (600 ms for the green channel).

Image processing vascular and neuronal measurements—Acquired time lapse two-photon images were analyzed in FIJI (Schindelin et al., 2012) and Matlab (version R2014b; MathWorks) using custom-written scripts. Images were first aligned to correct for motion in the x-y plane. Measurements in which the mouse had substantially moved were excluded from further analysis. In the vessel-containing images, regions of interest (ROIs) were drawn on several arteriolar segments (on average 2–3 per FOV) (Figure 1). Additional motion correction was performed when needed, by removing all frames that resulted in a >45% change in vessel diameter. Percentage vessel diameter change was determined by calculating vessel segment size for each frame (defined as the number of pixels per ROI occupied by the vessel) then subtracting by the average vessel segment size (over all frames) and dividing the difference by the average vessel segment size. A discrete Fourier transform was performed for each percentage vessel diameter trace and the power spectral density (PSD) of the cyclic vessel diameter oscillations was calculated in the range between 0.02–1 Hz. To compare the averaged hemodynamic response functions between Tg and WT mice, the PSD traces from several ROIs per vessel were averaged and plotted together, without additional smoothing. When making comparisons at specific frequencies (*e.g.* 0.1 Hz), the total amplitude of the PSD for the frequencies of interest was used. Within Tg mice, CAA burden for each ROI was measured on maximum intensity projections of the Z-stacks in the Methoxy-X04 channel (*i.e.* blue channel). Corresponding ROIs were first drawn on the dextran channel (*i.e.* green or red channel) and copied to the Methoxy-X04 channel blinded to CAA burden. CAA burden was then quantified for each ROI, after transforming the maximum intensity projection into a binary image, as the number of CAA positive pixels divided by total number of pixels within each ROI. In addition, CAA burden for the whole vessel was calculated separately to correlate with paravascular clearance rates. In the neuron-containing images, ROIs were drawn around each visible neuron on a maximum intensity projection of the time course (5 minutes). For each FOV, 1–2 additional ROIs were drawn in areas without neurons to correct for background fluorescent intensity (F_0). Percentage fluorescent intensity change was calculated per ROI as ($F - F_0 / F_0$) to generate Calcium traces. Neurons were visually classified as ON responders, OFF responders, NON responders, or Mixed responders based on their individual traces and averaged responses. A neuron was considered an ON responder when within 5 minutes >4 peaks of >20% change in fluorescent intensity were observed when the screen was on, resulting in a measurable response function in the averaged trace. An OFF responder showed >4 peaks of >20% change when the screen was off, whereas NON responders did not meet these criteria, and Mixed responders showed peaks both with the screen on and off. To compare the amplitude of ON responders between Tg and WT mice, the averaged traces were plotted together. The traces were smoothed using a moving average filter of length 5 frames.

Image processing paravascular clearance measurements—The evaluation of paravascular clearance rates was done blinded to stimulus paradigm (checkerboard or screen off). ROIs alongside arteries were picked manually in FIJI with the rectangle tool and positioned parallel to the vessel wall within the parenchyma, avoiding bends or bifurcations. The average fluorescent dextran intensity was calculated within each ROI for each frame over the entire time course and standardized to the intensity at time zero to generate relative intensity decay curves. Several summary measures were derived, including relative dextran

intensity at t=6, 12, and 18 minutes (to capture the three major phases of the decay curves), and area under the curve (AUC). In addition, one phase decay curves were fitted in Graphpad Prism (version 5.03) and R square values were calculated to assess goodness of fit for each condition. Clearance of unconjugated fluorescein was measured on maximum intensity projections.

Ex vivo tissue analysis—To quantify SMC density per vessel, maximum intensity images of the green channel were analyzed in FIJI, blinded to mouse ID, genotype, and CAA burden. ROIs were drawn outlining the SMC-positive surface arteriole. Next, a binary image was created, and SMC density was calculated as % SMC-positive pixels (*i.e.* (number of SMC positive pixels / number of pixels occupying the vessel ROI) × 100).

Quantification and Statistical Analysis

Fourier transform plots were generated in Matlab and presented with the power spectral density (1/Hz) on the y-axis and frequency (Hz) on the x-axis. To compare the amplitude of spontaneous vasomotion or evoked vascular reactivity, the local maximum power centered around 0.1 or 0.05 Hz was determined for each ROI and the maximum value among the ROIs from a single vessel was entered into the analysis. In addition, the sum of the power of the ultra-low frequency spectrum (0.02–0.4 Hz) was calculated for each ROI and the maximum value among the ROIs from a single vessel was entered into the analysis. Different vessels within the same mouse were considered independent. To create grouped hemodynamic response functions and grouped Fourier transform plots (in Matlab), multiple ROIs per vessel were averaged. Differences between genotype and conditions were compared using independent or paired student's t-tests for parametric measures. Linear correlations were calculated using Spearman's rank correlation coefficients. For visualization of the correlation plots, linear regression analysis was performed to generate fitting lines and R square values. All statistical analyses were performed in Graphpad Prism (version 5.03) and SPSS (version 22; IBM). No additional methods were used to determine whether the data met assumptions of the statistical approach. The statistical details of each experiment can be found in the Figure legends.

Data and Code Availability

The datasets and code supporting the current study have not been deposited in a public repository because imaging files are so large that they are not conducive to sharing but are available from the corresponding author on request.

Supplementary Material

Refer to Web version on PubMed Central for supplementary material.

Acknowledgments

The authors would like to thank Dr. Eloise Hudry for her help in setting up the experiments and Dr. Pankaj Karande for helpful discussions. This work was supported by the National Institutes of Health [R01 NS096730 to SMG and BJB; S10 RR025645, R01 EB000768, and RF1 NS110054 to BJB; K99 AG059893 to SJvV]. SJvV also received funding from the Netherlands Organization for Scientific Research during the period this work was performed (Rubicon fellowship 019.153LW.014 and Veni grant 91619021).

References

Absinta M, Ha SK, Nair G, Sati P, Luciano NJ, Palisoc M, Louveau A, Zaghloul KA, Pittaluga S, Kipnis J, et al. (2017). Human and nonhuman primate meninges harbor lymphatic vessels that can be visualized noninvasively by MRI. Elife 6, e29738. [PubMed: 28971799]

Albargothy NJ, Johnston DA, MacGregor-Sharp M, Weller RO, Verma A, Hawkes CA, and Carare RO (2018). Convective influx/glymphatic system: tracers injected into the CSF enter and leave the brain along separate periarterial basement membrane pathways. Acta. Neuropathol 136, 139–152. [PubMed: 29754206]

Aldea R, Weller RO, Wilcock DM, Carare RO, and Richardson G (2019). Cerebrovascular smooth muscle cells as the drivers of periarterial lymphatic drainage of the brain. Front. Aging. Neurosci 11, 1. [PubMed: 30740048]

Arbel-Ornath M, Hudry E, Eikermann-Haerter K, Hou S, Gregory JL, Zhao L, Betensky RA, Frosch MP, Greenberg SM, and Bacskai BJ (2013). Interstitial fluid drainage is impaired in ischemic stroke and Alzheimer's disease mouse models. Acta. Neuropathol 126, 353–364. [PubMed: 23818064]

Asgari M, de Zélicourt D, and Kurtcuoglu V (2016). Glymphatic solute transport does not require bulk flow. Sci. Rep 8, 38635.

Bakker EN, Bacskai BJ, Arbel-Ornath M, Aldea R, Bedussi B, Morris AW, Weller RO, and Carare RO (2016) Lymphatic clearance of the brain: perivascular, paravascular and significance for neurodegenerative diseases. Cell. Mol. Neurobiol 36, 181–194. [PubMed: 26993512]

Benveniste H, Liu X, Koundal S, Sanggaard S, Lee H, and Wardlaw J (2019). The glymphatic system and waste clearance with brain aging: a review. Gerontology 65, 106–119. [PubMed: 29996134]

Blaise R, Mateo V, Rouxel C, Zaccarini F, Glorian M, Béréziat G, Golubkov VS, and Limon I (2012). Wild-type amyloid beta 1–40 peptide induces vascular smooth muscle cell death independently from matrix metalloprotease activity. Aging Cell 11, 384–393. [PubMed: 22260497]

Brown LA, Key BJ, and Lovick TA (2002). Inhibition of vasomotion in hippocampal cerebral arterioles during increases in neuronal activity. Auton. Neurosci 10, 137–140.

Carare RO, Bernardes-Silva M, Newman TA, Page AM, Nicoll JA, Perry VH, and Weller RO (2008). Solutes, but not cells, drain from the brain parenchyma along basement membranes of capillaries and arteries: significance for cerebral amyloid angiopathy and neuroimmunology. Neuropath. Appl. Neurobiol 34, 131–144.

Charidimou A, Boulouis G, Gurol ME, Ayata C, Bacskai BJ, Frosch MP, Viswanathan A, and Greenberg SM (2017). Emerging concepts in sporadic cerebral amyloid angiopathy. Brain 140, 1829–1850. [PubMed: 28334869]

Chen TW, Wardill TJ, Sun Y, Pulver SR, Renninger SL, Baohan A, Schreiter ER, Kerr RA, Orger MB, Jayaraman V, et al. (2013). Ultrasensitive fluorescent proteins for imaging neuronal activity. Nature 499, 295–300. [PubMed: 23868258]

Christie R, Yamada M, Moskowitz M, and Hyman B (2001). Structural and functional disruption of vascular smooth muscle cells in a transgenic mouse model of amyloid angiopathy Am. J. Pathol 158, 1065–1071.

Davis J, Cribbs DH, Cotman CW, and Van Nostrand WE (1999). Pathogenic amyloid beta-protein induces apoptosis in cultured human cerebrovascular smooth muscle cells. Amyloid 6, 157–164. [PubMed: 10524279]

Diem AK, MacGregor Sharp M, Gatherer M, Bressloff NW, Carare RO, and Richardson G (2017). Arterial pulsations cannot drive intramural periarterial drainage: significance for Aβ drainage. Front. Neurosci 11, 475. [PubMed: 28883786]

Dirnagl U, Lindauer U, and Villringer A (1993). Nitric oxide synthase blockade enhances vasomotion in the cerebral microcirculation of anesthetized rats. Microvasc. Res 45, 318–323. [PubMed: 7686608]

Dumas A, Dierksen GA, Gurol ME, Halpin A, Martinez-Ramirez S, Schwab K, Rosand J, Viswanathan A, Salat DH, Polimeni JR, et al. (2012). Functional magnetic resonance imaging detection of vascular reactivity in cerebral amyloid angiopathy. Ann. Neurol 72, 76–81. [PubMed: 22829269]

Filosa JA, Bonev AD, and Nelson MT (2004). Calcium dynamics in cortical astrocytes and arterioles during neurovascular coupling. Circ. Res 95, e73–81. [PubMed: 15499024]

Garcia-Alloza M, Robbins EM, Zhang-Nunes SX, Purcell SM, Betensky RA, Raju S, Prada C, Greenberg SM, Bacskai BJ, and Frosch MP (2006). Characterization of amyloid deposition in the APPswe/PS1dE9 mouse model of Alzheimer disease. Neurobiol. Dis 24, 516–524. [PubMed: 17029828]

Hablitz LM, Vinitsky HS, Sun Q, Stæger FF, Sigurdsson B, Mortensen KN, Lilius TO, and Nedergaard M (2019). Increased glymphatic influx is correlated with high EEG delta power and low heart rate in mice under anesthesia. Sci. Adv 5, eaav5447. [PubMed: 30820460]

He Y, Wang M, Chen X, Pohmann R, Polimeni JR, Scheffler K, Rosen BR, Kleinfeld D, and Yu X (2018). Ultra-slow single-vessel BOLD and CBV-based fMRI spatiotemporal dynamics and their correlation with neuronal intracellular Calcium signals. Neuron 97, 925–939. [PubMed: 29398359]

Iadecola C, Zhang F, Niwa K, Eckman C, Turner SK, Fischer E, Younkin S, Borchelt DR, Hsiao KK, and Carlson GA (1999). SOD1 rescues cerebral endothelial dysfunction in mice overexpressing amyloid precursor protein. Nat. Neurosci 2, 157–161. [PubMed: 10195200]

Iadecola C (2017). The neurovascular unit coming of age: a journey through neurovascular coupling in health and disease. Neuron 96, 17–42. [PubMed: 28957666]

Iliff JJ, Wang M, Zeppenfeld DM, Venkataraman A, Plog BA, Liao Y, Deane R, and Nedergaard M (2013). Cerebral arterial pulsation drives paravascular CSF-interstitial fluid exchange in the murine brain. J. Neurosci 33, 18190–18199. [PubMed: 24227727]

Jankowsky JL, Slunt HH, Ratovitski T, Jenkins NA, Copeland NG, and Borchelt DR (2001). Co-expression of multiple transgenes in mouse CNS: a comparison of strategies. Biomol. Eng 17, 157–165. [PubMed: 11337275]

Jäkel L, Van Nostrand WE, Nicoll JAR, Werring DJ, and Verbeek MM (2017). Animal models of cerebral amyloid angiopathy. Clin. Sci 131, 2469–2488. [PubMed: 28963121]

Kelly P, Hudry E, Hou SS, and Bacskai BJ (2018). In vivo two photon imaging of astrocytic structure and function in Alzheimer's disease. Front. Aging. Neurosci 10, 219. [PubMed: 30072889]

Kimbrough IF, Robel S, Roberson ED, and Sontheimer H (2015). Vascular amyloidosis impairs the gliovascular unit in a mouse model of Alzheimer's disease. Brain 138, 3716–3733. [PubMed: 26598495]

Kress BT, Iliff JJ, Xia M, Wang M, Wei HS, Zeppenfeld D, Xie L, Kang H, Xu Q, Liew JA, et al. (2014). Impairment of paravascular clearance pathways in the aging brain. Ann. Neurol 76, 845–861. [PubMed: 25204284]

Kuchibhotla KV, Wegmann S, Kopeikina KJ, Hawkes J, Rudinskiy N, Andermann ML, Spires-Jones TL, Bacskai BJ, and Hyman BT (2014). Neurofibrillary tangle-bearing neurons are functionally integrated in cortical circuits in vivo. Proc. Natl. Acad. Sci. U. S. A 111, 510–514. [PubMed: 24368848]

Louveau A, Smirnov I, Keyes TJ, Eccles JD, Rouhani SJ, Peske JD, Derecki NC, Castle D, Mandell JW, Lee KS, et al. (2015). Structural and functional features of central nervous system lymphatic vessels. Nature 523, 337–341. [PubMed: 26030524]

Love S, Chalmers K, Ince P, Esiri M, Attems J, Jellinger K, Yamada M, McCarron M, Minett T, Matthews F, et al. (2014). Development, appraisal, validation and implementation of a consensus protocol for the assessment of cerebral amyloid angiopathy in post-mortem brain tissue. Am. J. Neurodegener. Dis 3, 19–32. [PubMed: 24754000]

Mateo C, Knutsen PM, Tsai PS, Shih AY, and Kleinfeld D (2017). Entrainment of arteriole vasomotor fluctuations by neural activity is a basis of Blood-Oxygenation-Level-Dependent "resting-state" connectivity. Neuron 96, 936–948. [PubMed: 29107517]

Mestre H, Tithof J, Du T, Song W, Peng W, Sweeney AM, Olveda G, Thomas JH, Nedergaard M, and Kelley DH (2018). Flow of cerebrospinal fluid is driven by arterial pulsations and is reduced in hypertension. Nat. Commun 9, 4878. [PubMed: 30451853]

Niwa K, Younkin L, Ebeling C, Turner SK, Westaway D, Younkin S, Ashe KH, Carlson GA, and Iadecola C (2000). Abeta 1–40-related reduction in functional hyperemia in mouse neocortex

during somatosensory activation. Proc. Natl. Acad. Sci. U. S. A 97, 9735–9740. [PubMed: 10944232]

Noordmans HJ, van Blooijs D, Siero JCW, Zwanenburg JJM, Klaessens JHGM, and Ramsey NF (2018). Detailed view on slow sinusoidal, hemodynamic oscillations on the human brain cortex by Fourier transforming oxy/deoxy hyperspectral images. Hum. Brain. Mapp 39, 3558–3573. [PubMed: 29693304]

Osol G, and Halpern W (1988). Spontaneous vasomotion in pressurized cerebral arteries from genetically hypertensive rats. Am. J. Physiol 254, H28–33. [PubMed: 3337256]

Rayshubskiy A, Wojtasiewicz TJ, Mikell CB, Bouchard MB, Timerman D, Youngerman BE, McGovern RA, Otten ML, Canoll P, McKhann GM 2nd., et al. (2014). Direct, intraoperative observation of ~0.1 Hz hemodynamic oscillations in awake human cortex: implications for fMRI. Neuroimage 87, 323–331. [PubMed: 24185013]

Park L, Zhou J, Zhou P, Pistick R, El Jamal S, Younkin L, Pierce J, Arreguin A, Anrather J, Younkin SG, et al. (2013). Innate immunity receptor CD36 promotes cerebral amyloid angiopathy. Proc. Natl. Acad. Sci. U. S. A 110, 3089–3094. [PubMed: 23382216]

Park L, Koizumi K, El Jamal S, Zhou P, Previti ML, Van Nostrand WE, Carlson G, and Iadecola C (2014). Age-dependent neurovascular dysfunction and damage in a mouse model of cerebral amyloid angiopathy. Stroke 45, 1815–1821. [PubMed: 24781082]

Peca S, McCreary CR, Donaldson E, Kumarpillai G, Shobha N, Sanchez K, Charlton A, Steinback CD, Beaudin AE, Flück D, et al. (2013). Neurovascular decoupling is associated with severity of cerebral amyloid angiopathy. Neurology 81, 1659–1665. [PubMed: 24097810]

Peng W, Achariyar TM, Li B, Liao Y, Mestre H, Hitomi E, Regan S, Kasper T, Peng S, Ding F, et al. (2016). Suppression of glymphatic fluid transport in a mouse model of Alzheimer's disease. Neurobiol. Dis 93, 215–225. [PubMed: 27234656]

Schindelin J, Arganda-Carreras I, Frise E, Kaynig V, Longair M, Pietzsch T, Preibisch S, Rueden C, Saalfeld S, Schmid B, et al. (2012). Fiji: an open-source platform for biological-image analysis. Nat. Methods 9, 676–682. [PubMed: 22743772]

Schley D, Carare-Nnadi R, Please CP, Perry VH, and Weller RO (2006). Mechanisms to explain the reverse perivascular transport of solutes out of the brain. J. Theor. Biol 238, 962–974. [PubMed: 16112683]

Smith AJ, Yao X, Dix JA, Jin BJ, and Verkman AS (2017). Test of the 'glymphatic' hypothesis demonstrates diffusive and aquaporin-4-independent solute transport in rodent brain parenchyma. Elife 6, e27679. [PubMed: 28826498]

Sweeney MD, Sagare AP, and Zlokovic BV (2018). Blood-brain barrier breakdown in Alzheimer's disease and other neurodegenerative disorders. Nat. Rev. Neurol 14, 133–150. [PubMed: 29377008]

Van Opstal AM, Van Rooden S, Van Harten T, Ghariq E, Labadie G, Fotiadis P, Gurol ME, Terwindt GM, Wermer MJH, Van Buchem MA, et al. (2017). Cerebrovascular function in presymptomatic and symptomatic individuals with hereditary cerebral amyloid angiopathy: a case-control study. Lancet. Neurol 16, 115–122. [PubMed: 27989553]

Vinters HV (1987). Cerebral amyloid angiopathy. A critical review. Stroke 18, 311–324. [PubMed: 3551211]

Vonsattel JP, Myers RH, Hedley-Whyte ET, Ropper AH, Bird ED, and Richardson EP Jr. (1991).Cerebral amyloid angiopathy without and with cerebral hemorrhages: a comparative histological study. Ann. Neurol 30, 637–649. [PubMed: 1763890]

Wang P, and Olbricht WL (2011). Fluid mechanics in the perivascular space. J. Theor. Biol 274, 52–57. [PubMed: 21241713]

Weller RO, Massey A, Kuo YM, and Roher AE (2000). Cerebral amyloid angiopathy: accumulation of A beta in interstitial fluid drainage pathways in Alzheimer's disease. Ann. N. Y. Acad. Sci 903, 110–117. [PubMed: 10818495]

Weller RO, and Nicoll JA (2003). Cerebral amyloid angiopathy: pathogenesis and effects on the ageing and Alzheimer brain. Neurol. Res 25, 611–616. [PubMed: 14503015]

Weller RO, Boche D, and Nicoll JA (2009). Microvasculature changes and cerebral amyloid angiopathy in Alzheimer's disease and their potential impact on therapy. Acta. Neuropathol 118, 87–102. [PubMed: 19234858]

Winder AT, Echagarruga C, Zhang Q, and Drew PJ (2017). Weak correlations between hemodynamic signals and ongoing neural activity during the resting state. Nat. Neurosci 20, 1761–1769. [PubMed: 29184204]

Wojtas AM, Kang SS, Olley BM, Gatherer M, Shinohara M, Lozano PA, Liu CC, Kurti A, Baker KE, Dickson DW, et al. (2017). Loss of clusterin shifts amyloid deposition to the cerebrovasculature via disruption of perivascular drainage pathways. Proc. Natl. Acad. Sci. U. S. A 114, 6962–6971.

Xie L, Kang H, Xu Q, Chen MJ, Liao Y, Thiyagarajan M, O'Donnell J, Christensen DJ, Nicholson C, Iliff JJ, et al. (2013). Sleep drives metabolite clearance from the adult brain. Science 342, 373–377. [PubMed: 24136970]

Zipfel GJ, Han H, Ford AL, and Lee JM (2009). Cerebral amyloid angiopathy: progressive disruption of the neurovascular unit. Stroke 40, S16–19. [PubMed: 19064794]

Highlights

- Spontaneous low frequency oscillations can be observed in arterioles in awake mice
- Vasomotion drives paravascular clearance of solutes from the brain
- Paravascular clearance is impaired in the context of cerebral amyloid angiopathy

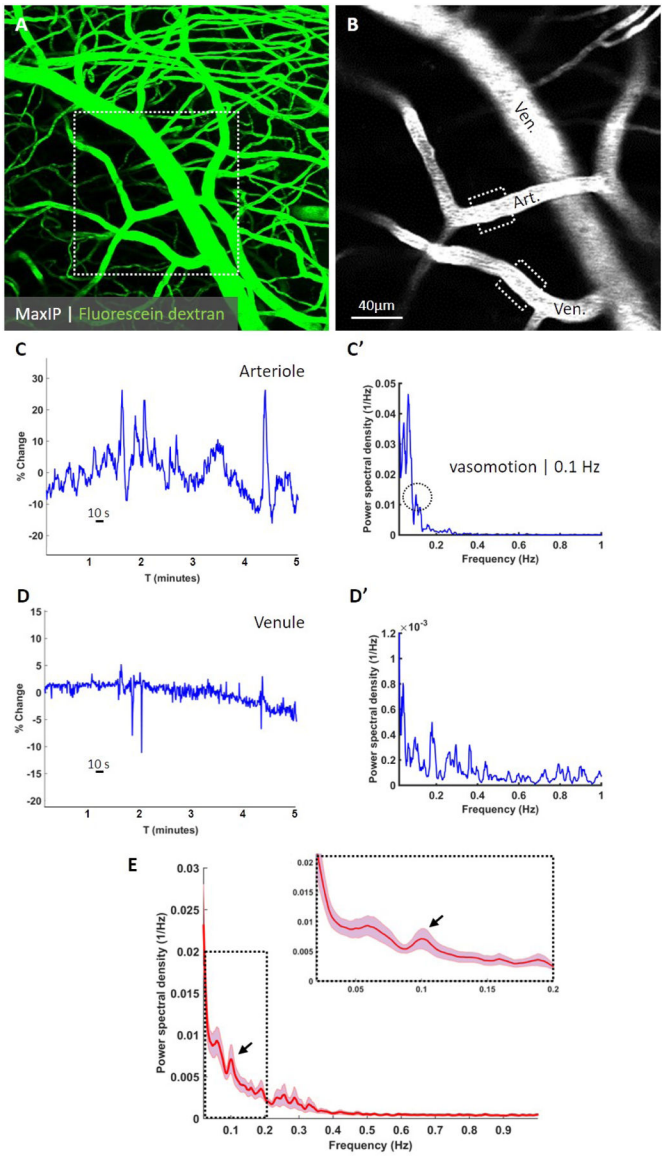

Figure 1. Spontaneous vasomotion (around 0.1 Hz) can be observed in arterioles in the awake mouse brain.

Representative *in vivo* two-photon microscopy image of a fluorescent angiogram through a cranial window in an awake head-fixed wild-type mouse (A). Resting-state spontaneous activity is recorded in arterioles over a 5-minute time course at 2x magnification and a frame rate of ~2 Hz (B). Spontaneous dilations and constrictions in the arteriolar segment outlined in panel B are visualized as percentage vessel diameter change over the recorded 5-minute time course (C). Note: the two highest observed peaks correspond to movement-induced arteriolar dilations. Fourier transform analysis of the time-course in panel C reveals arteriolar oscillations in the ultra-low frequency range, with a distinct peak at 0.1 Hz, also known as vasomotion (C'). Note: in some cases an additional peak could be observed at even lower frequencies, potentially related to movement-induced arteriolar dilations. Spontaneous vasomotion is not observed in venules (DD'). The averaged Fourier plot across wild-type mice (n=14 arterioles in 8 mice (for each arteriole ~3 ROIs were averaged))

revealed a broad range of ultra-low frequencies (<0.4 Hz) with a distinct peak centered at around 0.1 Hz, but no peaks in the range 0.4–1 Hz (E). Shaded areas in E represent standard error of the mean.

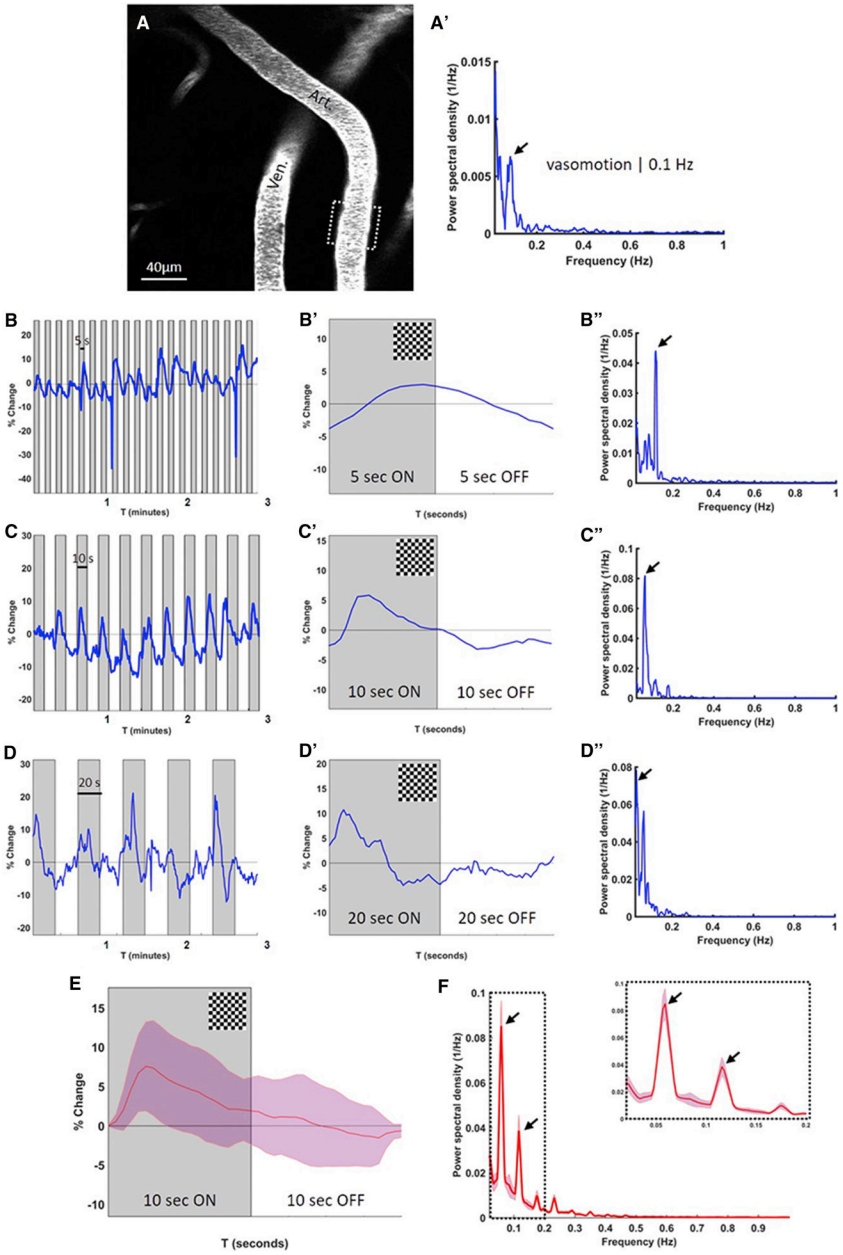

Figure 2. Evoked vascular reactivity can be driven at different frequencies of visual stimulation.

Spontaneous vasomotion is observed in an arteriole in an awake head-fixed wild-type mouse (AA'). Visual stimulation in the form of a flashing checkerboard results in evoked vascular reactivity (functional hyperemia), following distinct patterns of presentation. Presenting the flashing checkerboard pattern for 5 seconds (ON) followed by 5 seconds grey screen (OFF) repeatedly results in vasodilations once every 10 seconds (B), a distinct averaged hemodynamic response function (B') and a peak in the Fourier distribution at 0.1 Hz (B"). Presenting the checkerboard for 10 seconds (ON) followed by 10 seconds grey screen (OFF) results in a peak at 0.05 Hz (CC'C"), and 20 seconds (ON) followed by 20 seconds (OFF) results in a peak at 0.025 Hz (DD'D"). Note: only the first three minutes of the total 5-minute recordings are shown in panel B, C, and D for optimal presentation of the individual

traces. The averaged hemodynamic response function across wild-type mice (n=17 arterioles in 9 mice (for each arteriole ~3 ROIs were averaged)) reveals that the 10 seconds checkerboard ON/OFF presentation reproducibly evokes on average a vessel diameter change of ~7% (E). The corresponding averaged Fourier plot shows a prominent peak at 0.05 Hz (the stimulation frequency) as well as a smaller peak at 0.1 Hz (the vasomotion frequency) (F). Shaded areas in E represent standard deviations. Shaded areas in F represent standard error of the mean.

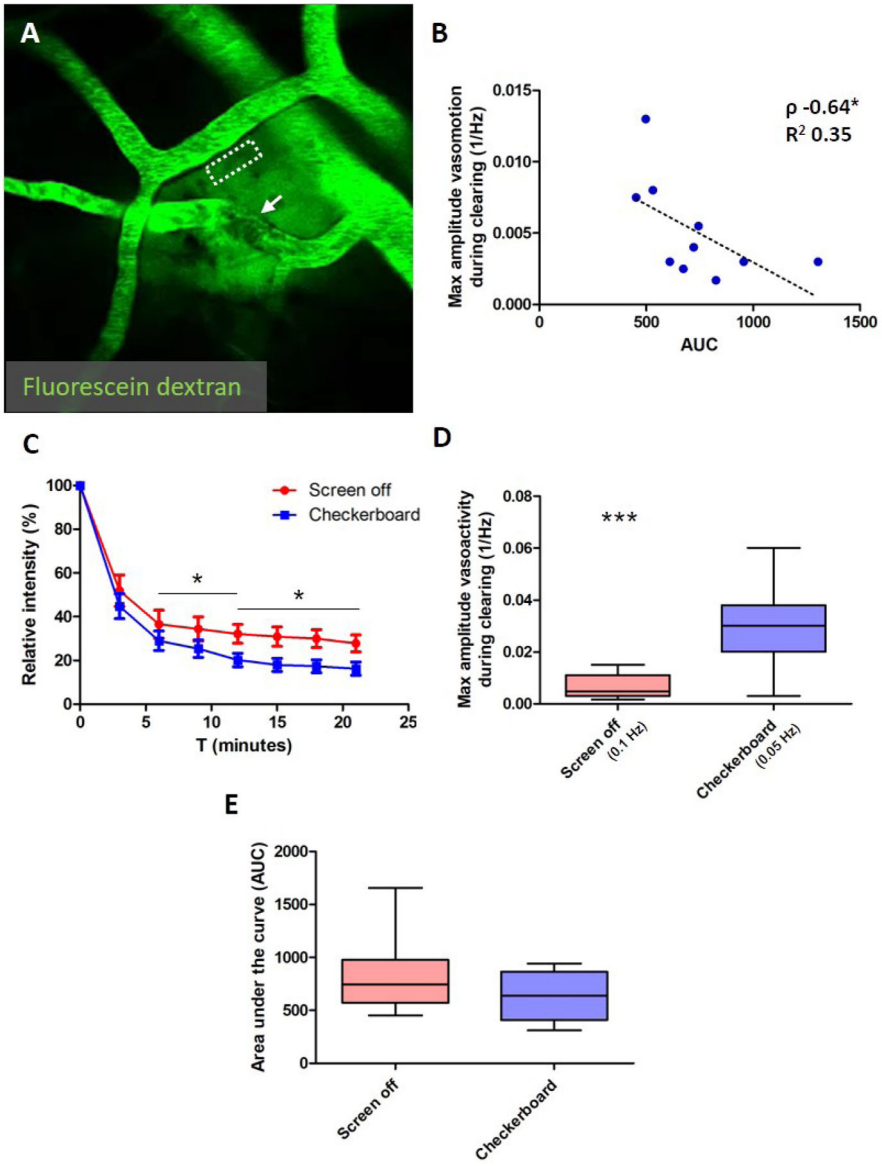

Figure 3. Paravascular clearance rate is associated with vasomotion in wild-type mice.

Clearance of extravasated fluorescent dextran can be measured non-invasively in awake head-fixed mice alongside arteries (dashed ROI) with two-photon microscopy after laser irradiation of neighboring vessels (A; arrow indicates clotting reaction that immediately occurs after the local vessel irradiation). The maximum amplitude of the spontaneous vasomotion (expressed as the power of the peak at 0.1 Hz) per vessel during clearing correlates with the area under the fluorescein dextran decay curve (AUC) (B; Spearman's ρ −0.64, p=0.049, n=10 vessels in 8 wild-type mice). Note: two measurements were excluded from this analysis due to extensive leakage after laser irradiation. Visual stimulation during the period of extravasated fluorescein dextran clearance resulted in faster clearance rates (C), and can be explained by the significant increase in vasoactivity as quantified by the maximum amplitude of the evoked vascular reactivity (expressed as the power of the peak at 0.05 Hz) per vessel compared to the maximum amplitude of the spontaneous vasomotion

(expressed as the power of the peak at 0.1 Hz) when the screen was off (D; 0.027 ± 0.016 1/Hz with visual stimulation (n=11 vessels) vs. 0.0065 ± 0.0046 1/Hz without (n=12 vessels), t-test, p=0.0003). Faster clearances during visual stimulation was quantified as significantly lower relative dextran intensities at t=12 minutes (C; 20.1 ± 10.3 % with visual stimulation (n=11 vessels in 7 mice) vs. 32.2 ± 15.6 % without visual stimulation (n=13 vessels in 9 mice), t-test, p=0.038) and t=18 minutes (C; 17.5 ± 9.7 % with visual stimulation vs. 30.0 ± 14.9 % without visual stimulation, t-test, p=0.026) and AUC (F; 638 ± 226 with visual stimulation vs. 839 ± 341 without, t-test, p=0.11). Error bars in C represent standard error of the mean. Median and range are indicated in D and E. * $p<0.05$, *** $p<0.001$.

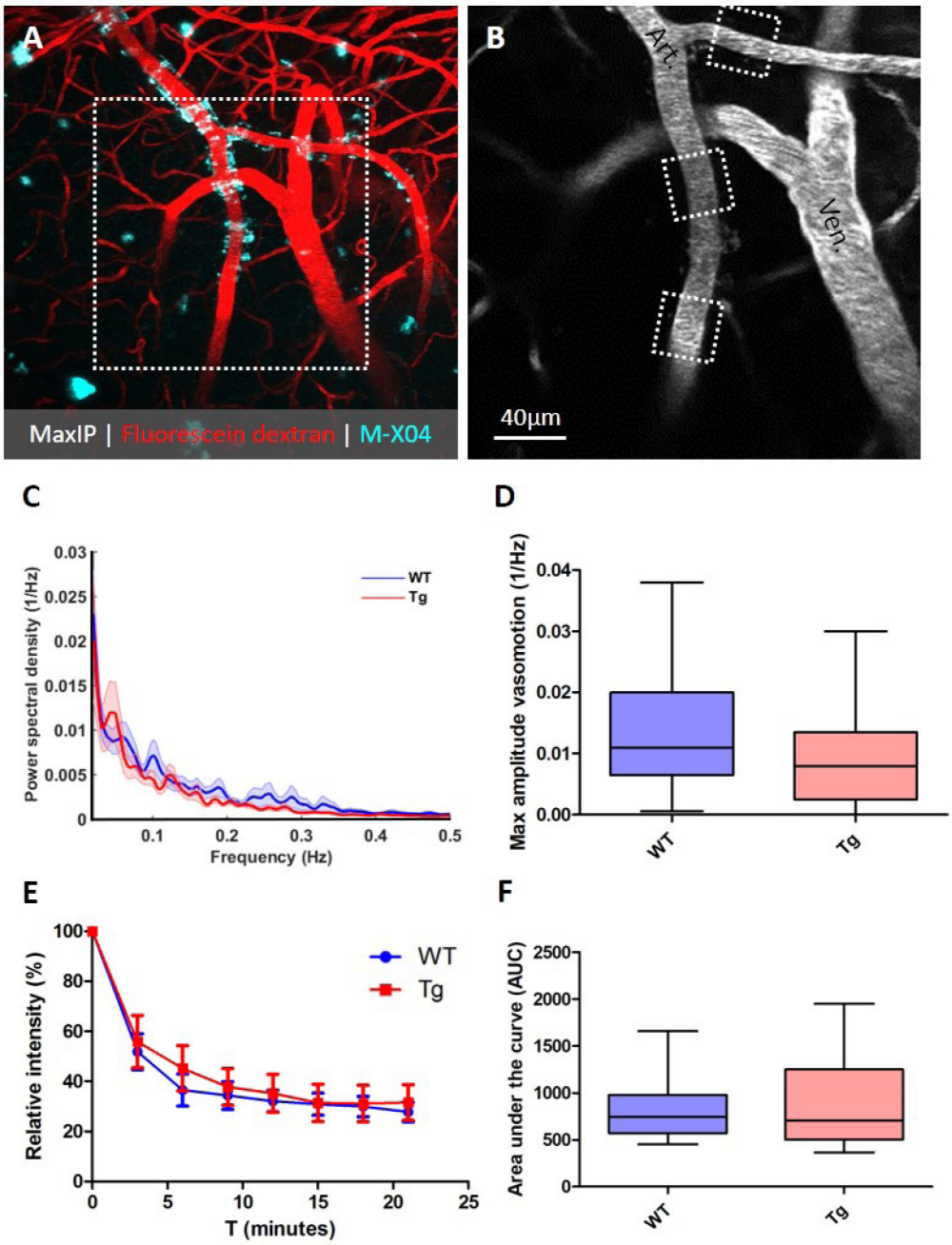

Figure 4. Spontaneous vasomotion (at 0.1 Hz) and baseline paravascular clearance are not altered in 8–10 months old APP/PS1 mice.

Representative *in vivo* two-photon microscopy image of a fluorescent angiogram through a cranial window in an awake head-fixed transgenic (Tg) APP/PS1 mouse (A). Intraparenchymal Aβ plaques and vascular Aβ depositions (CAA) are visualized through Methoxy-X04, an intraperitoneally injected fluorescent Congo Red derivative that crosses the blood-brain barrier and binds to Aβ. Note: fluorescein dextran is depicted in red for better contrast with Aβ in cyan. Spontaneous vasomotion in Tg mice is recorded in arterioles over a 5-minute time course at 2x magnification and a frame rate of ~2 Hz (B), and is

comparable to wild-type (WT) animals (D; maximum amplitude at 0.1 Hz was 0.0094 ± 0.0083 1/Hz in Tg (n=13 vessels in 4 mice) vs. 0.014 ± 0.010 1/Hz in WT mice (n=14 vessels in 8 mice), t-test, p=0.29). The combined Fourier plot shows the averaged frequency distributions (after averaging several ROIs per vessel) in the range 0.02 – 0.5 Hz for WT and Tg mice (C). Note: three vessel measurements from Tg mice were excluded from the averaged plot because no peaks were observed <0.5 Hz. Paravascular clearance decay curves are comparable between WT (n=12 vessels in 8 mice) and Tg mice (n=11 vessels in 4 mice) (E), quantified as area under the curve (F; 839 ± 341 in WT vs. 908 ± 510 in Tg, t-test, p=0.70). Shaded areas in C and error bars in E represent standard error of the mean. Median and range are indicated in D and F.

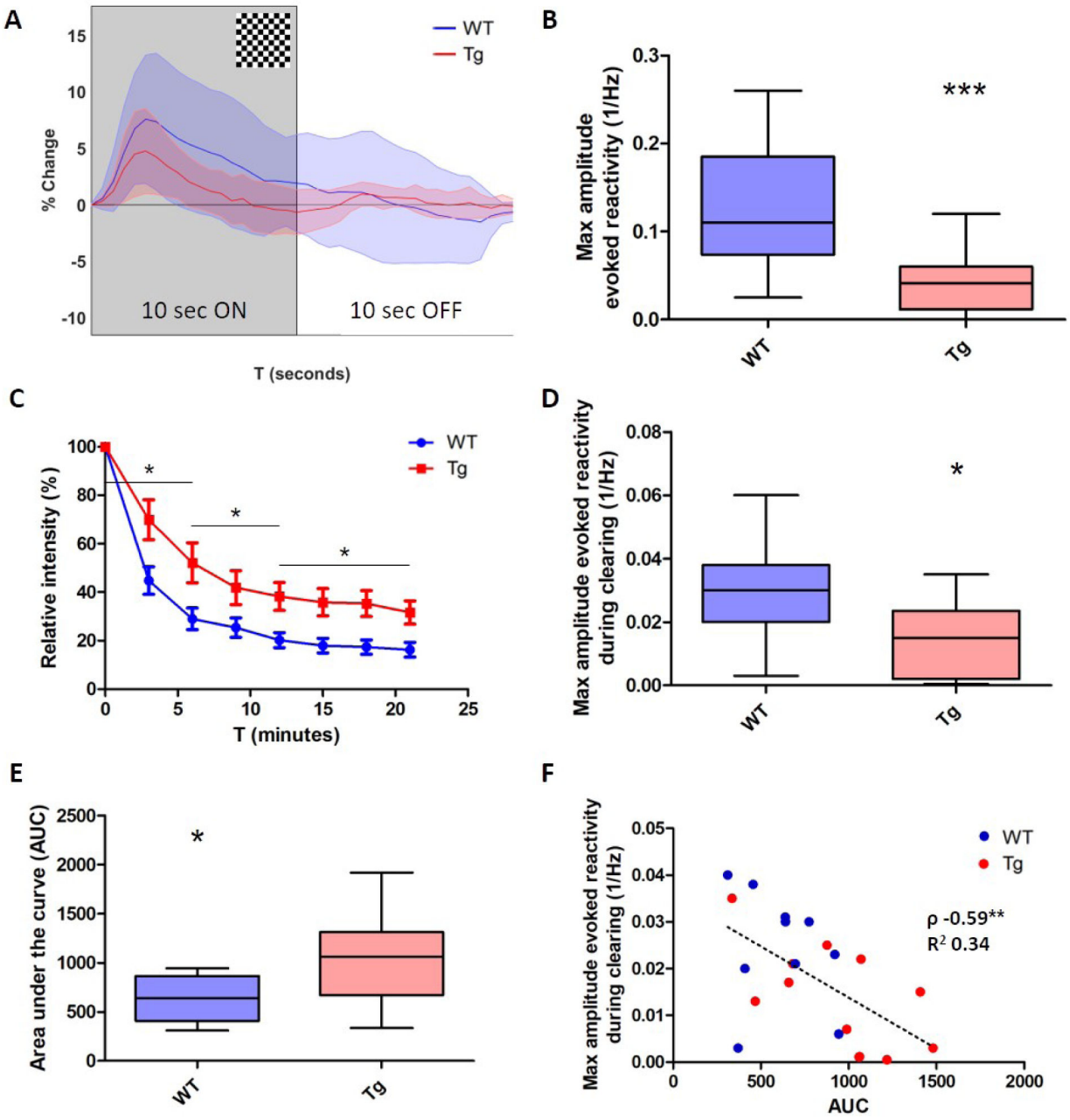

Figure 5. Evoked vascular reactivity and paravascular clearance rates are reduced during visual stimulation in 8–10 months old APP/PS1 mice.

Evoked vascular reactivity upon visual stimulation is impaired in transgenic (Tg) mice compared to wild-type (WT) mice, as visualized by the averaged hemodynamic response functions (A; shaded areas represent standard deviations), and the quantification of the maximum amplitude of the power at 0.05 Hz after Fourier transform (B; 0.043 ± 0.034 1/Hz (n=22 vessels in 5 mice) in Tg vs. 0.13 ± 0.069 1/Hz (n=18 vessels in 9 mice) in WT mice, t-test, $p<0.0001$). Visual stimulation during the period of extravasated fluorescein dextran clearance resulted in slower clearance rates in Tg compared to WT mice (C), and can be explained by the significant difference in evoked vascular reactivity as quantified by the

maximum amplitude (expressed as the power of the peak at 0.05 Hz) per vessel (D; 0.015 ± 0.012 1/Hz (n=13 vessels in 5 mice) in Tg vs. 0.027 ± 0.016 1/Hz (n=11 vessels in 7 mice) in WT mice, t-test, p=0.033). Quantification of the fluorescein dextran decay curves revealed significantly slower clearance rates during visual stimulation in Tg compared to WT mice, as expressed by area under the curve (AUC) (E; 1017 ± 433 in Tg vs. 638 ± 226 in WT, t-test, p=0.016). The maximum amplitude of the evoked vascular reactivity during clearance significantly correlated with AUC (F; Spearman's ρ −0.59, p=0.0041). Note: two outliers were removed from the correlation to enable reliable curve fitting, but even without removing them the correlation remained significant (p=0.028). Error bars in C represent standard error of the mean. Median and range are indicated in B, D, and E. * p<0.05, ** p<0.01, *** p<0.001.

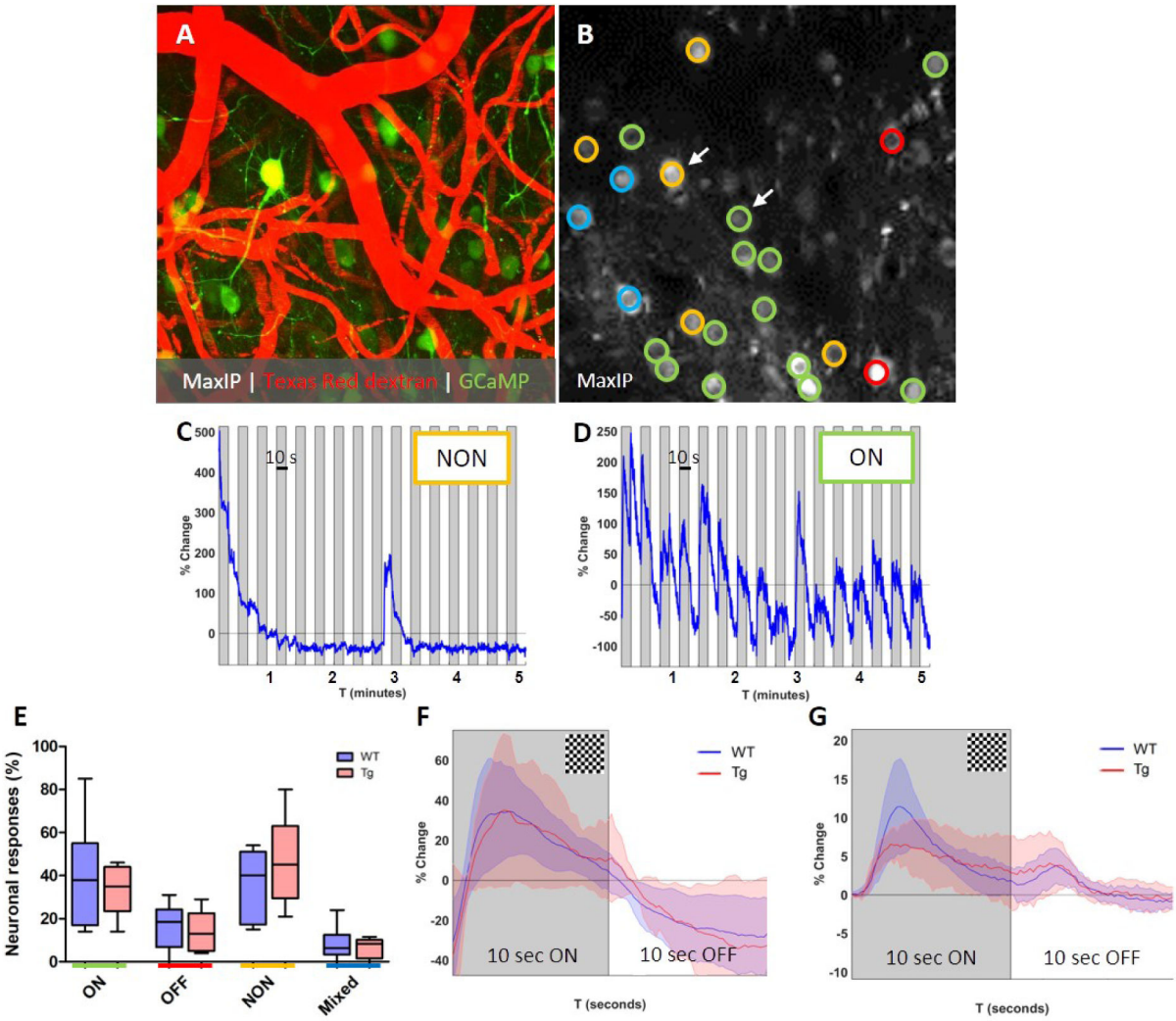

Figure 6. Reduced vascular reactivity in APP/PS1 mice is not driven by altered neuronal responses.

Representative *in vivo* two-photon microscopy image of a fluorescent angiogram with GCaMP6S expressing neurons through a cranial window in an awake head-fixed wild-type (WT) mouse (A). Evoked neuronal reactivity in WT and Tg mice is recorded over a 5-minute time course at 2x magnification and a frame rate of ~5 Hz (B). Neurons were classified as ON (green), OFF (red), NON (yellow), or Mixed (blue) responders based on their individual and averaged traces (B). Representative trace of an individual NON responder (C; arrow in B) and an individual ON responder (D; arrow in B). No significant differences were observed in average percentage of ON responders (p=0.67), OFF responders (p=0.65), NON responders (p=0.38), or Mixed responders (p=0.64) between WT (total number of 200 neurons in 6 mice) and Tg mice (total number of 178 neurons in 5 mice) (t-tests) (E). Also, no difference was observed between the averaged shape of the percentage signal change in ON responders, between WT (72 ON responders) and Tg mice (55 ON responders) (F). Yet, evoked vascular reactivity was significantly impaired in the same Tg mice compared to WT (G; vascular recordings in these mice were done at the same

resolution and frame-rate as neuronal recordings). Shaded areas in panels F and G represent standard deviations. Median and range are indicated in E.

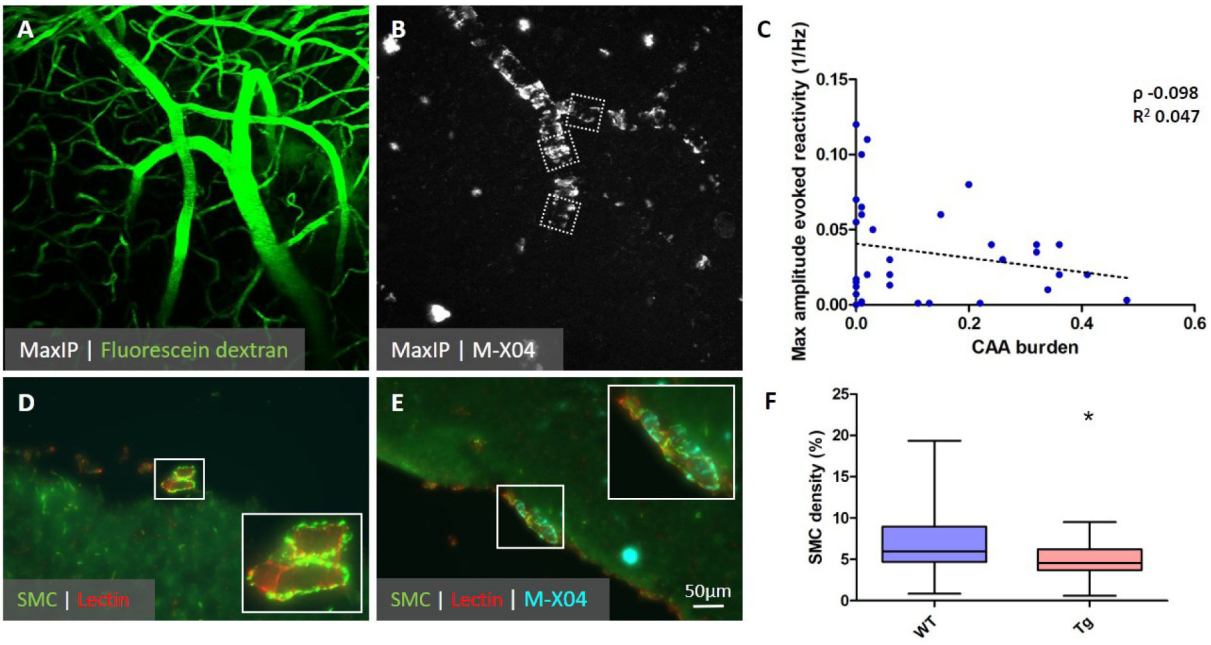

Figure 7. Reduced vascular reactivity in APP/PS1 mice is not associated with local CAA burden, but with loss of vascular smooth muscle cells.

Representative *in vivo* two-photon microscopy image of a fluorescent angiogram through a cranial window in an awake head-fixed transgenic (Tg) APP/PS1 mouse (A). Intraparenchymal Aβ plaques and vascular Aβ depositions (CAA) are visualized through Methoxy-X04, an intraperitoneally injected fluorescent Congo Red derivative that crosses the blood-brain barrier and binds to Aβ (B). CAA burden was quantified on the maximum intensity projections of the Methoxy-X04 channel and correlated with the amplitude of the evoked vascular reactivity, quantified as the maximum peak at 0.05 Hz in 8–10 months old transgenic mice. No significant correlation was found between CAA burden and evoked vascular reactivity per vessel segment (C; Spearman's ρ −0.098, p=0.58, n=35 vessel segments in 5 mice). Smooth muscle cell (SMC) density was quantified with *ex vivo* immunohistochemistry in brain sections of 18 months old wild-type (WT) and Tg mice that underwent *in vivo* two-photon microscopy. Representative images of pial surface arterioles in WT (D) and Tg (E) mice are shown, which suggest loss of SMCs in CAA-positive vessels. After excluding three vessels that did not exhibit any CAA from the Tg group, SMC density was found to be significantly reduced in Tg (4.9 ± 2.0 %, n=25 vessels in 6 mice) compared to WT mice (7.1 ± 4.1 %, n=34 vessels in 8 mice, t-test, p=0.016) (F). Median and range are indicated in F. * $p<0.05$.

KEY RESOURCES TABLE

REAGENT or RESOURCE	SOURCE	IDENTIFIER
Antibodies		
Monoclonal Mouse Anti-Human Smooth Muscle Actin	Agilent	Cat#M-0851
Goat anti-mouse Alexa Fluor 488	Thermo Fisher Scientific	Cat#A-11001
Bacterial and Virus Strains		
AAV1.Syn.GCaMP6s.WPRE.SV40	UPenn Vector core	N/A
Chemicals, Peptides, and Recombinant Proteins		
Methoxy-X04	Glixx Laboratories Inc.	CAS#863918-78-9
70 kDa fluorescein Dextran	Invitrogen	Cat#D-1823
70 kDa Texas Red Dextran	Invitrogen	Cat#D-1830
DyLight 594 labeled Lycopersicon Esculentum (Tomato) Lectin	Vector Laboratories	Cat#DL-1177
CdSSe/ZnS core/shell QDs with PEG	Ocean Nanotech LLC	Cat#QMG-450–02
Fluorescein sodium salt	Sigma-Aldrich	Cat#F6377
Experimental Models: Organisms/Strains		
C57BL/6J mice	Jackson Laboratories	Stock#000664
B6C3-Tg(APPswe,PSEN1dE9)85Dbo/Mmjax mice	Jackson Laboratories	Stock#34829-JAX
B6.Cg-Tg(Myh11-cre,-EGFP)2Mik/J mice	Jackson Laboratories	Stock#007742
Software and Algorithms		
MATLAB	Mathworks	R2014b-R2016a
FIJI	Schindelin et al. Nat Methods 2012	ImageJ 1.52e
Graphpad Prism	www.graphpad.com	Version 5.03
SPSS	IBM	Version 22